Simulation of LHCb RICH 2025/26 Testbeam Investigating SiPM and FastRICH Upgrades

C. A. Joynes
cj1g21@soton.ac.uk

School of physics and astronomy,
University of Southampton,
Southampton,
SO17 1BJ,
United Kingdom

May 29, 2025

Abstract

The aim of the 2025/26 RICH Testbeam is to investigate the advantages of the SiPM and the FastRICH chip, which will be implemented in future LHCb upgrades. This thesis created simulations for two of the Testbeam setups used to investigate these components.

Initially, a simulation of the October 2025 Testbeam was created. The resulting occupancy plots of this show that SiPMs (75% occupancy) outperform the currently used MaPMTs (50% occupancy). Then a different, larger lens was simulated to compare to the current lens in the setup. The larger 200 mm lens had a greater angular resolution of 4.68 mrad, compared to 4.85 mrad, but caused the occupancy to decrease by 14% for all detectors. The differences between the lenses were insufficient to justify buying a new lens and therefore it was recommended to stick with the smaller 150 mm lens. To complete the October study, timing data were simulated for the Testbeam. At thresholds of 9.8 μA and lower, there was negligible time walk. However, at thresholds above 17.5 μA, a time walk of 350 ps was observed, which increased with threshold.

Next, a design for the April 2026 Testbeam was simulated. This Testbeam will use a gas radiator instead of a lens, as this will drastically improve the Cherenkov angular resolution. Several different designs were investigated, but in the end a 1000 mm gas chamber of C_4F_{10}, with the optical components aligned along the beam line, was proposed to the Testbeam team. This setup had occupancy of 35% along the ring arc and Cherenkov angular resolution of 0.315 mrad. When a beam width of 6 mm was included, there was no impact on the results. Unfortunately, replacing the radiator material with CF_4, a gas with a lower refractive index, did not work in the proposed design and would require a chamber of 1700 mm in length. Finally, the design was tested at low momenta in proton synchrotron conditions of 8 GeV. This produced an angular resolution of 0.398 mrad and an occupancy that remained at 35%, which was good enough to justify using proton synchrotron conditions. The results demonstrated that the design can use non-saturated tracks and opens the possibility of particle identification in Testbeams.

Contents

1 Introduction **4**

2 Background **5**
- 2.1 CP Violation . . . 5
- 2.2 RICH detectors . . . 5
- 2.3 LHCb detector Upgrades and Testbeam . . . 7
- 2.4 Silicon Photomultipliers . . . 7
- 2.5 FastRICH Electronic Chip . . . 8
- 2.6 Time Walk . . . 8
- 2.7 Simulations . . . 9

3 Methodology **10**
- 3.0.1 RICH Errors . . . 10
- 3.1 Simulating the Current 2025 Testbeam . . . 10
  - 3.1.1 Building Simulation Objects . . . 10
  - 3.1.2 Cherenkov Production . . . 11
  - 3.1.3 Quantum Efficiency and Hit Acceptance . . . 12
  - 3.1.4 Beam Width . . . 13
- 3.2 Alternative Lens Options . . . 13
- 3.3 Timing Data and Readout . . . 14
  - 3.3.1 Time-of-Acquisition against Time-over-Threshold . . . 14
  - 3.3.2 Amplitude Curve Models . . . 14
  - 3.3.3 2024 Testbeam Readout Data . . . 15
- 3.4 Simulating a Gas Chamber and Cryostat Testbeam . . . 15
  - 3.4.1 Benefits of a Gas Chamber and Cryostat . . . 15
  - 3.4.2 Fixed Parameters and restrictions . . . 16
  - 3.4.3 Proposed Setup Models . . . 16
  - 3.4.4 Two Mirror: Research and Development . . . 17
  - 3.4.5 Additional Implications . . . 18
  - 3.4.6 RICH Reconstruction . . . 19

4 Results and Discussion **20**
- 4.1 Results from the 2025 Testbeam Study . . . 20
  - 4.1.1 Quantum Efficiency Curves of Different Photodetectors . . . 20
  - 4.1.2 Occupancy of the Setup . . . 21
- 4.2 Comparing 25-713 Lens to 25-709 Lens . . . 23
  - 4.2.1 Comparing Occupancies . . . 23
  - 4.2.2 Comparing Cherenkov Angle Resolution . . . 24
  - 4.2.3 Beam Width Result . . . 24
- 4.3 Simulated Readout and Timing Data . . . 25
  - 4.3.1 Which of the Models was Better . . . 25
  - 4.3.2 Investigating ToA vs ToT plots . . . 25
- 4.4 Results and discussion of Cryostat and Gas Chamber Investigation . . . 27
  - 4.4.1 Model comparisons . . . 27
  - 4.4.2 Further Study into the Two Mirror Setup . . . 30
  - 4.4.3 Beam Width and Beam Divergence Results . . . 32
  - 4.4.4 Testing different Radiator Gases . . . 34
  - 4.4.5 No 1-Hit Protocol . . . 35
  - 4.4.6 PS Conditions . . . 35

5 Conclusion **36**
- 5.1 Conclusion - October 2025 Testbeam Simulation . . . 36
- 5.2 Conclusion - April 2026 Testbeam Simulation . . . 36

6 Further Research and Development **36**

1 Introduction

CERN has the world's largest particle accelerator with a circumference of 26.7 km [1]. In this ring are four independent experiments, LHCb, ATLAS, ALICE and CMS, which aim to complete or reinvent the standard model. Unlike both the ATLAS and CMS experiments, the LHCb was designed as a specialist detector for flavour physics, searching for why there is more matter than antimatter in the universe. Here beauty quarks are produced in high-energy Proton-Proton (pp) collisions, within energy ranges of $\sqrt{7}\ TeV$ and $\sqrt{13}\ TeV$. Knowledge of b-quark yield is important for calculating the sensitivity of experiments measuring CP-violation and rare decays [2]. It was the first detector to observe the mixing of neutral charm mesons ($D^0 \leftrightarrow \bar{D}^0$) within a single measurement [3]. To measure and observe these collisions, the LHCb has specialist detectors. The key detectors are the Vertex Locator detector (VELO) and its Ring Imaging Cherenkov (RICH) detectors, which measure charged particle tracks and identify different types of particles, respectively [4].

With improving understanding and technology, these detectors need to be upgraded to enhance the precision of the results. However, before an upgrade is installed into the massive experiment, rigorous testing on the new upgrade must be completed to verify that it will work as intended in the high-luminosity environment. This testing is completed in a Testbeam, which is a highly controlled beam that exposes the upgrades to extreme conditions similar to those in the actual experiment.

The aim of this thesis was to produce simulations of the 2025/26 Testbeam, to simulate the expected spatial and timing data using the SiPM and FastRICH chip upgrades. The October 2025 Testbeam setup will use a lens to create Cherenkov photons and focus them onto the photodetectors. By plotting the hits detected and verifying their efficiencies, the new SiPM was compared to the current MaPMTs to determine whether the SiPM was a better candidate for the RICH detector. An alternative lens was also investigated to determine whether this would improve Testbeam results. Furthermore, by plotting ToA against ToT, the time walk of the system was simulated. Next, a new design for the Testbeam setup was investigated. The current lens design does not exploit the full potential of the SiPM detectors. Instead, a cryostat and gas chamber setup will be designed and used in the 2026 Testbeam. A gas radiator produces a much smaller Cherenkov angular resolution which can be utilised by the SiPM. Several designs were investigated, and using reconstruction, the spatial data and resolution of each design were calculated to determine which gas chamber setup was best. Some final variations to this design were also investigated including alternative beam parameters and radiator materials.

Acronym	**Definition**	**Acronym**	**Definition**
LHC	Large Hadron Collider	ROC	Radius of Curvature
LHCb	Large Hadron Collider beauty experiment	LS3	Long Shutdown 3
HL-LHC	High-Luminosity Large Hadron Collider	LS4	Long Shutdown 4
VELO	Vertex Locator	QE	Quantum Efficiency
RICH	Ring Imaging Cherenkov	FPGA	Field Programmable Gate Arrays
CPT	Charge, Parity, Time symmetry	TTS	Transit Time Spread
CKM	Cabibbo-Kobayashi-Maskawa	VL	Versatile Link
SiPM	Silicon Photomultiplier	ToA	Time of Acquisition
MaPMT	Multi-anode Photomultiplier Tube	ToT	Time over Threshold
HPD	Hybrid Photon Detectors	CFD	Constant Fraction Discriminator
PID	Particle Identification	HPE	Hits Per Event
C_4F_{10}	Perfluorobutane	PS	Proton Synchrotron
CF_4	Tetrafluoromethane	SPS	Super Proton Synchrotron

Table 1: Table of Acronyms

2 Background

2.1 CP Violation

Charge-Parity violation occurs when physical laws do not remain the same under a CPT symmetry; the combined transformation of charge conjunction, C, parity inversion, P, and time reversal, T. CPT theory states that under mild technical assumptions any unitary, local, Lorentz-invariant quantum field within flat Minkowski space is CPT invariant [5], and this should apply to the Standard Model.

Quarks can transition between flavours with probabilities outlined by the Cabibbo-Kobayashi-Maskawa (CKM) matrix. The entries of the CKM matrix roughly follow a power scaling in $\lambda \approx 0.22$, so a popular approximation is the Wolfenstein parametrization,

$$V_{CKM} = \begin{pmatrix} V_{ud} & V_{us} & V_{ub} \\ V_{cd} & V_{cs} & V_{cb} \\ V_{td} & V_{ts} & V_{tb} \end{pmatrix} = \begin{pmatrix} 1-\lambda^2/2 & \lambda & A\lambda^3(\rho - i\eta) \\ -\lambda & 1-\lambda^2/2 & A\lambda^2 \\ A\lambda^3(1-\rho-i\eta) & -A\lambda^2 & 1 \end{pmatrix} + O(\lambda^4). \quad (1)$$

The Wolfenstein approximation has three real parameters, λ, A, ρ and an imaginary η. The complex phase η, within the CKM matrix, gives rise to processes that decay at different rates for particles and antiparticles that would violate the charge-parity symmetry.

The LHCb experiment found evidence of CP violation of statistical significance in decay $\Lambda_b^0 \rightarrow p\pi^-\pi^+\pi^-$, which showed a difference between matter and antimatter baryons [6].

2.2 RICH detectors

To detect these imbalances between matter and antimatter the LHCb uses RICH detectors, designed around Cherenkov radiation, a discovery made in 1934 by the Russian scientist Pavel Alekseevich Cherenkov, in which he observed luminescence in solutions when under gamma radiation. Cherenkov had observed a conical wavefront with normal at an angle θ to the velocity of the particle moving in the solution.

$$cos(\theta) = \frac{c}{vn} \quad (2)$$

where v is the speed of the charged particle, n is the refractive index of the medium and c is the speed of light. Given $cos\theta$ cannot exceed one, for any real angle, it follows that a moving charged particle in a medium would only create a conical wave when,

$$v > \frac{c}{n}. \quad (3)$$

or when the particles speed exceeds that of the phase speed of light [7].

High quality Particle Identification (PID) is essential for almost all precise flavour physics measurements. Cherenkov radiation is used in high energy detectors at the LHCb, because it can provide a clear way to identify particles in a large momentum range of about 2-100GeV. Plots of Cherenkov angle and particle momentum are made, with different particle types creating different and distinguishable plots which are used to verify them.

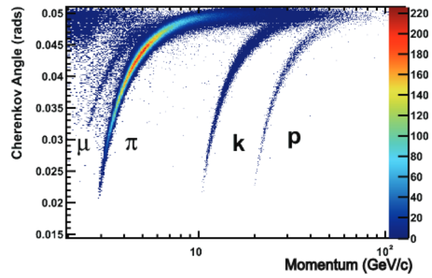

Figure 1: Cherenkov angle vs track momentum in a C_4F_{10} radiator [8]

Given that the relationship between Cherenkov angle and a particle's velocity is limited by the refractive index, and hence the material in which the particle emits the Cherenkov radiation, material choice is very important when it comes to detectors. An ordinary transparent dielectric would not work for conventional Cherenkov detectors as these materials have refractive indexes much higher than 1, where the Cherenkov angle would saturate and become independent of the velocity of the particle [9]. Instead aerogel, C_4F_{10} and CF_4 gas radiators are/have been used in detectors and have refractive indexes of 1.03, 1.0013 and 1.0004 respectively, for visible light ranges [10].

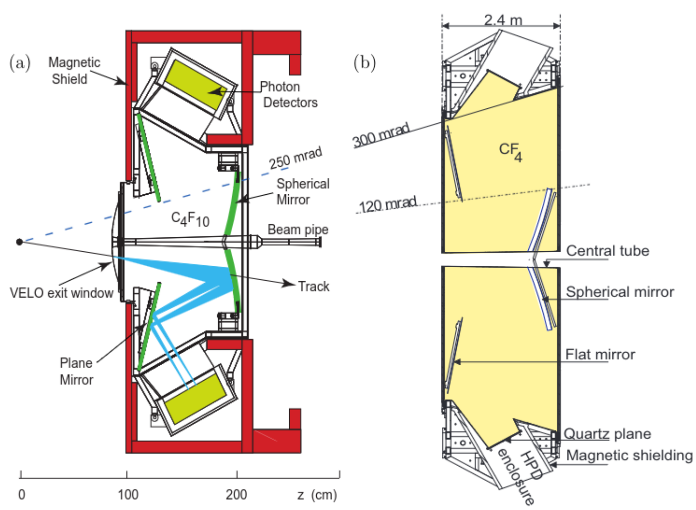

Figure 2: (a) RICH 1 and (b) RICH 2 schematic side view [11]

Each RICH detector has a single gas radiator, C_4F_{10} and CF_4 for RICH 1 and RICH 2 respectively. The beam is aligned in the Z-axis direction. Upstream of the dipole magnet is RICH 1 which is optimised for low momentum particles within the range $10GeV - 65GeV$, where as RICH 2 is located downstream of the magnet and optimised for high momentum ranges up to $100GeV$. From [Figure 2], it is clear that both detectors have two mirrors on either side of the beam line, one a spherical mirror and the other a flat mirror. The RICH 1 spherical mirror has a Radius Of Curvature (ROC) of 2700 mm. The RICH 2 has an ROC of 8600 mm that is tilted ±450 mrad with respect to the X-axis, with the aim of focusing the particles into a ring. The flat mirror has a tilt of ±140 mrad with respect to the X-axis and aims to focus the particles onto the detectors [12].

Previously in the LHCb RICH detectors, Hybrid Photon Detectors (HPDs) were used to capture 200-600nm wavelength photons. HPDs had a window of $2.5 \times 2.5\ mm^2$, a 32×32 pixel array, and high speed, with a 25ns timing resolution. Electron-hole pairs are created on average 1 for every 3.6eV deposited from incoming photons [13]. Although HPDs provide a number of advantages, such as signal definition and linearity, they are complex and have a huge number of readout channels that require cost-optimized solutions [14]. Long Shutdown 2 of the LHC brought upgrades to the RICH detectors, which was important in improving the readout rate from 1 MHz to 40 MHz. The additional challenging requirements and conditions of this upgrade required a new type of sensor, Multianode Photo Multiplier Tubes (MaPMT). These have an 8×8 array of 64 dynode chains that are enveloped by vacuum [15]. MaPMTs are smaller and have a simpler readout than HPDs. During Run3 the detector readout chain consisted of MaPMTs read out by CLARO ASIC chip which were then connected to the Versatile Links (VL) by the digital board interface. Field Programmable Gate Arrays (FPGA) capture the digital signals from the CLARO chips, formats the data, and transmits it to the VL at a rate of $320Mb/s$. Run3 is limited by the clocking resource as well as the radiation hardness of the design. FPGAs have a poor radiation hardness, which means that the use of logic resources in Run3 is limited to reduce the probability of radiation upsets [16]. Malfunction or disturbance of electronics in a system due to the effect of ironizing radiation is referred to as radiation upset and can be minor, such as causing bits to flip in memory to major with total electronic burnouts.

2.3 LHCb detector Upgrades and Testbeam

Between 2026 − 2030 there is a planned shutdown of the LHC, Long Shutdown 3 (LS3) [17], during which many of the detectors and sub-detectors will receive improvements and overhauls. The main aims of LS3 are to introduce fast timing and prepare the detectors for High Luminosity LHC (HL-LHC) where the LHC will operate at much higher luminosities with an increased number of collisions. Then after some more data taking, there is another period for maintenance and improvements during Long Shutdown 4 (LS4), which will be 2034 − 2035. LS4 will introduce Upgrade II which is expected to increase luminosity to more than 7 times that of Run3 and turn the system into HL-LHC. To align with the increase in luminosity, a significant improvement in the design readouts will also be required. The aim is to reach a $1Gb/s$ sampling rate within the electronics.

Improvements to any hardware require rigorous testing before it is installed. To complete these tests, a Testbeam is setup. Testbeams are highly controlled beams of particles that are used to expose components to LHC environments. The component can then be tested, validated and calibrated for use in true high energy collisions. To maintain performance with the increase in luminosity expected after upgrade II, an improvement in the precision of both the spatial and time coordinates of the RICH detectors is required. The RICH 2025/26 Testbeam is tasked with testing two main new components which should help to provide this increase in precision; Silicon Photomultipliers (SiPM) and the FastRICH readout chip.

2.4 Silicon Photomultipliers

The spatial improvement will hopefully come with upgrade II in LS4, as there is no current device that meets all requirements of the LHCb. However, it is anticipated that the SiPMs under development will be suitable when it is time to make the change. Given the large increase in luminosity that is expected to come with the general upgrades to the LHC, components with much better radiation hardness and durability are being investigated. Compared to current MaPMTs, the SiPMs seem more suitable for this high luminosity environment [18] with greater radiation hardness. Additionally, SiPMs have a quantum efficiency (QE) spectrum which can be shifted into longer wavelengths, which can reduce the chromatic error from the Cherenkov radiation. They also have a high average QE then both MaPMTs and HPDs and work within magnetic fields, meaning there is no need for magnet shielding which could reduce weight and costs. The RICH teams are hoping for a reduction in pixel size to $1 \times 1\ mm^2$ that would improve pixel error. Increased luminosity will require extremely fast detectors, to handle the larger volume of hits, with LHCb setting a requirement that all new detectors must have a work rate of at least 40 MHz, and ideally a timing resolution of 100ps or better [19].

The SiPMs improvements will help with the development of timing coordinates; however, true development will come from the installation of the FastRICH chip.

2.5 FastRICH Electronic Chip

the FastRICH Chip is readout ASIC, planned to be integrated within LS3, and would allow the new systems to timestamp each individual photon into 25ps time bins [17], within a 2ns time gate. This improvement comes with limited cost and prepares for Upgrade II.

Including timestamping will allow smaller time gates to be chosen and combining this with the MaPMT Transit Time Spread (TTS) of $\sigma \sim 150\ ps$ gives an optimal time gate of 600 ps. A narrower gate reduces performance by removing signal photons but a wider gate would increase the amount of background noise detected.

2.6 Time Walk

Electronic chips read the signal from the photomultipliers to create an amplitude curve where a threshold is then applied. The "Delay time" is the time at which the threshold is crossed, whilst the time walk is how this Delay time varies with signal amplitude. Time walk introduces another spread in timing data that increases time resolution and can cause signal loss [20]. Currently, with the CLARO chip, and using an external resistor, the input bias current can be increased which can reduce the effect of time walk by a factor of 2 at the cost of a greater power consumption of 1.5mW per channel.

CLARO can take the Time-over-Threshold (ToT), and use it to perform a time walk correction which is fed into the FPGA as it has flexible logic. Alternatively, With FastRICH, time walk can be corrected by using Constant Fraction Discrimination (CFD), which would therefore mean that no ToT information would need to be transmitted and the hardware shutter time could be narrower than that of the current CLARO chip, further reducing bandwidth requirements.

CFD works by taking the threshold at a constant fraction of the maximum pulse height, resulting in a delay time which is independent of the pulse height removing time walk.

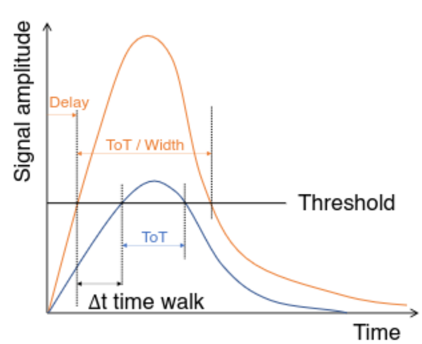

Figure 3: Time walk is introduced by the variation of the amplitude curve for a fixed threshold

2.7 Simulations

At the LHC simulations are used from CMS to ATLAS to LHCb, often being utilized in similar ways, by allowing a deep understanding of the complex detectors performance before runs take place. Simulations are used at the LHC to provide a detailed theoretical reference, which experimental data can be compared too and models of known and new physics can be tested against [21]. In high energy particle physics, simulations are used to simulate particles from single events and then running over this thousands of times to get a distribution. Physical parameters and construction conditions will be stored within a database that allows for identical simulation and reconstruction processes [22].

At CERN, the simulation software used is Geant4, a powerful and flexible toolkit which can be tailored for a wide range of applications. Researchers can extend Geant4 with custom features and integrate it with other software tools such as ROOT. The software has built-in support for modelling particle interactions of a large energy range and was optimized for high performance simulations. It is capable of running in parallel across multiple processors, which is important when scaling up simulations to larger datasets, necessary for LHC simulations. CERN was instrumental to the development of Geant4, combining with physicists from KEK to create the software back in 1993 [23], and so it is deeply integrated into the culture, support and improvement of the organization. In fact a main motivation behind the initial creation of Geant4 was the heavy ion experiment at the LHC and the large functionality it required.

3 Methodology

The 2025/26 RICH Testbeam has 3 slots. The first is in late May 2025, the second is in October 2025 and the third and final is in April 2026.

This thesis is Split into two main parts, the first is a simulation study for the October 2025 slot. This study is to simulate the current setup, which will look at testing the SiPM and FastRICH chip using a lens setup, and is covered in sections: (3.1), (3.2), (3.3). The second part is to design a gas chamber for a new setup which will use a gas radiator and cryostat and will be used in the April 2026 slot. This is covered in section (3.4).

3.0.1 RICH Errors

There are 3 main sources of error that affect the Cherenkov angle measurements made in RICH detectors. These errors must be minimised and made equal in order to attain the highest performance from the setup.

$$\sigma_{tot} = \sqrt{\sigma_{chr}^2 + \sigma_{pix}^2 + \sigma_{emp}^2} \quad (4)$$

where σ_{tot} is the total resolution of the Cherenkov angle, σ_{chr} is the resolution due to chromatic error, σ_{emp} is resolution due to emission point error, and σ_{pix} is the resolution due to pixel error [24].

The chromatic error is caused by different wavelengths of light having different refractive indices for the same medium [25]. And given that the Cherenkov angle depends on the refractive index, as seen in (equation 2), different wavelengths will have different Cherenkov angles, producing a spread in the data with a value σ_{chr}.

Pixel error is due to the size of the pixels of the detectors. Photodetectors cannot identify where within the detector the actual hit is, but instead assume that the hit was detected in the centre of the pixel. Therefore, there is an error on that hit depending on the size of the pixel, which produces a spread in the data equal to σ_{pix}.

Lastly is the emission point error, which is dependant on the optical geometry of the setup. The position of the emission point of the Cherenkov photon will have an error associated with it. This is because photodetectors not in the focal plane; mirrors with large tilt distorting rings into ellipticities; mirrors with small ROC causing spherical aberrations, all produce a spread in the data, characterised by σ_{emp}.

The aim is to reduce these independent resolutions so that the overall resolution is minimised and the measurements are more precise. Because of (equation 4), if the errors are not of equal size, the larger error will dominate and cause almost all the uncertainty in the readings.

3.1 Simulating the Current 2025 Testbeam

A simulation of the October 2025 Testbeam will provide expected data for the experiment to compare with. Simulating different setups will also allow us to optimise the Testbeam design.

3.1.1 Building Simulation Objects

To begin, measurements supplied by manufacturers or made precisely within the laboratory on site were taken, and accurate reconstructions of the components were made inside the simulation. Testbeam schematics were then used to replicate the setup, traditionally the beam line runs along the Z-axis, with the components also sat along this axis in the 2025 setup. Important geometries in this setup included the radiator, which consisted of a lens and a mirror, the overarching support structure which encased the 3 Elementary Cells (EC) and of course the 5 photodetectors themselves. The lens was made of N-BK7 substrate, a type of borosilicate crown glass with a refractive index of 1.516 [26], which meant that there was poor resolution between particle types. This was not an issue, as the Testbeam study is not concerned with PID but rather testing the capabilities of the SiPM and FastRICH. The positioning of these components in the simulation can be seen in [Figure 4]. The setup for 2025 includes two SiPMs, two 1-inch MaPMTs and a single 2-inch MaPMT. In the 2025 Testbeam, the main option is to use a plano-convex lens to create and direct the Cherenkov radiation, as it is cheap and easy to implement, and has been used previously in prior Testbeams from 2014. The lens, as seen in [Figure 5], was created by combining both a radiator component and a mirrored surface. Within the radiator, the particle, which was a pion in this simulation, undergoes Cherenkov radiation, which was then totally internally reflected off the flat surface, remaining inside the lens. This radiation then reflects off the mirror component and was directed out of the lens and towards the detectors which are placed within the focal plane.

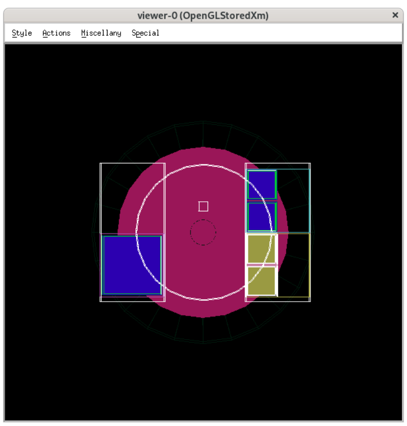

Figure 4: looking down the beam line, Radiator lens (pink) with the 2-inch MaPMT (navy left), the 1-inch MaPMTs (navy right) and the SiPMs (green).

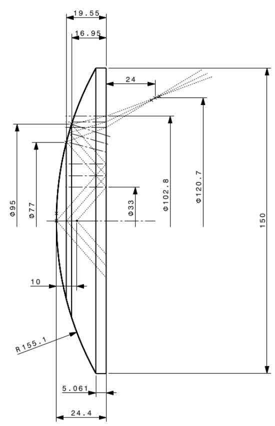

Figure 5: Manufacturers Schematic drawing of the plano-convex lens, Cherenkov radiation is totally internally reflected of the flat surface and then reflected out[27].

3.1.2 Cherenkov Production

Cherenkov radiation produced photons of varying energy and therefore varying wavelength as well. Within the simulation these photons are produced using a Poisson distribution with a mean value of 400 nm. The plot of these wavelengths, seen in [Figure 6] resembles the distribution in which they are created. As highlighted in section(3.0.1), this variation in wavelengths will cause a chromatic error in the results. It was therefore important to understand the distribution of the wavelengths of the photons to understand the impact this had on the results.

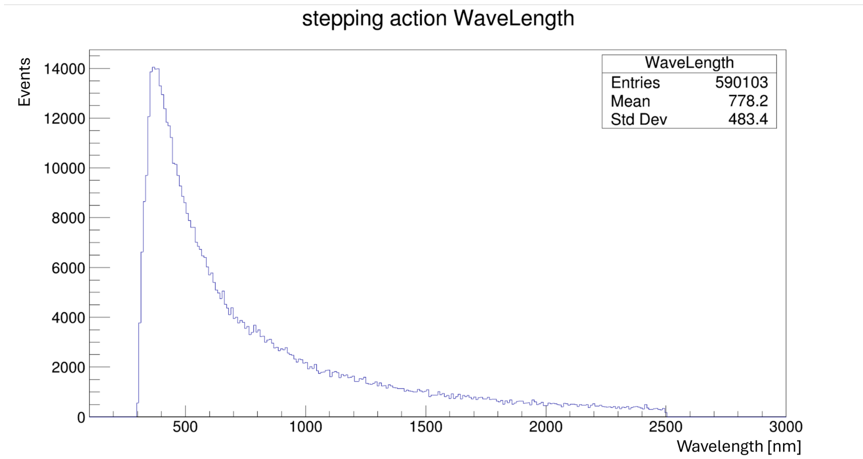

Figure 6: Plot indicated the wavelengths of the produced Cherenkov Photons, with 590,000 photons produced in 100 events.

This plot showed that photons were produced within the range $300nm$ to $2500nm$, this was because any photons smaller than this are absorbed by the radiator material. The majority of the photons fall within $300nm - 900nm$ and therefore this was the most important range to consider. These photons were mainly of the visible light range.

3.1.3 Quantum Efficiency and Hit Acceptance

It was important to know where the peak mean wavelength of the distribution was because the photodetectors each have a Quantum Efficiency (QE),

$$QE = \frac{I_{em}}{I_{abs}}, \tag{5}$$

where I_{em}, is the number of photoelectrons emitted by the detector, and I_{abs} is the number of photons absorbed by the detector [28].

The QE is the fraction of photons that are converted into photoelectrons in the photodetector, and is an intrinsic property of each detector and supplied by the manufacturer, and additionally tested and measured in the laboratory on site at CERN. Once a hit was detected in the simulation, the corresponding QE curve for that detector was sampled to check if that hit was accepted or not.

Along with QE acceptance, the simulation would also test another trigger that determined if a hit was accepted or not. In a given event, each pixel of a photodetector had a binary response, either it had detected a hit (1) or it had not detected anything (0), therefore, it does not matter if one or three photons hit a single pixel in a given event, the response would still be a single hit (1). This was coded into the simulation so that for any pixels consecutively hit in a single event, the consecutive hit would not be accepted. This had been coded as a flag so that it could easily be turned on or off, which allowed observations of how many true hits (all accepted) reach the detector plane compared to how many the simulation accepts (only first hit).

Given that the geometries had been created and placed inside the simulation, the physics had been encoded and the hit criteria was established, The simulation could then replicate and return spatial data that would be expected from the Testbeam. For timing data, the transit time and readout must also be added, which is covered in [section 3.3].

3.1.4 Beam Width

Additionally, a 5 mm beamwidth was added, which created a variation in the direction the action particle follows based on a normal distribution. The aim of which was to more accurately simulate the initial conditions of the Testbeam as the beam does not enter the lens perfectly along the axis every time, and this addition should reduce any discrepancies between the simulated data and Testbeam data because of this effect.

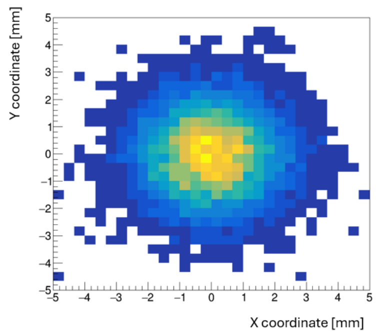

Figure 7: Plot shows the XY position in which the beam enters the radiator, The bright yellow indicates a high number of hits whilst blue is a low number of hits

3.2 Alternative Lens Options

The Testbeam team worked closely together and discussions had begun about whether a larger lens would be a better option. This was because a larger lens should produce a larger Cherenkov ring which would move the components further away from the beam line, which could reduce noise and error. Additionally, a larger lens should have reduced aberration and therefore greater Cherenkov resolution. The current lens 27-509, which had been used in previous Testbeam setups, had a radius of 150 mm. The next lens, 27-513, had a radius of 200 mm. Both are seen in the schematics [Figure 8]. To test this theory, the team wanted a simulation of the lens to be completed and compared with the smaller lens to see which would make a better choice for the 2025 Testbeam.

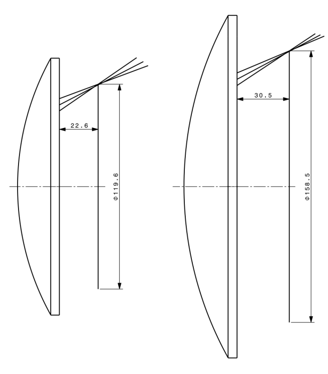

Figure 8: The current lens being used in the simulation, lens 27-509 (left), then the suggested larger lens 27-513 (right) [29].

3.3 Timing Data and Readout

The 2025 Testbeam aims to demonstrate the effects of the SiPM and FastRICH chips implementations; which includes the improvements to both spatial and timing data. So far, the thesis has only investigated the improvements to the spatial data through the use of the SiPM. There is also an improvement to timing data that needs to be included in the simulations. These improvements come from both, the SiPM and its increased work rate over the MaPMTs as well as from the new FastRICH chip and its ability to place hits into narrow bins allowing tighter time cuts and reducing noise. This section will cover how these improvements to the timing data were implemented.

3.3.1 Time-of-Acquisition against Time-over-Threshold

Plotting Time-of-Acquisition (ToA) against ToT showed the amount of time walk within the system. ToA was the time from when the hit was detected to when it had been fully processed by the readout chain, and as such there were several independent timing steps which make up the ToA value for a given hit:

$$ToA = \text{Deposit time} + \text{Transit time} + \text{Delay time} \tag{6}$$

Firstly, Deposit time, which refers to the initial time in which the Cherenkov photon hit the photodetector.

Then Transit time, which is defined as the time interval between the photon hitting the cathode, creating a photoelectron, and the readout of the output signal [30]. Transit Time Spread (TTS) is the deviation in the Transit time of a photomultiplier and is important because it is TTS that impacts the jitter of the Transit time and therefore ToA. Readings of the Transit time and TTS for the specific PMTs that are used in the Testbeam were taken at CERN in the lab. The laboratory reported an average Transit time of $3.7ns$ and a TTS of $150ps$ for the 1-inch MaPMT and $140ps$ for the 2-inch MaPMT. Within the simulation, a Gaussian distribution was created using the laboratory measurements and can be sampled to apply a Transit time to each individual hit.

Finally, a Delay time is required and as seen within section (2.6), the electronic chips were fed an amplitude curve, from the photodetectors, which had a threshold value cut across it, creating a Delay time and ToT value. Both were dependant on the amplitude curve, which will vary for each channel of a photomultiplier, given its relation to the gain of a given hit. Gain measurements within the lab demonstrated a channel with a gain of $140\ \mu A \pm 60\ \mu A$. For simplicity within the simulation, only this single channel was taken to create a Gaussian distribution, from which gains were sampled. Using the gain of each hit, two models were created to simulate the curve.

3.3.2 Amplitude Curve Models

The gain curves seen in section (2.6), had exponential tails. To accurately create this curve, the first model used a difference-of-exponentials function which took rise time and fall time parameters to replicate the shape. However, if the threshold was above the section of the curve that begins to tail off, then the curve followed a Gaussian shape. Therefore, the second model used a Gaussian function to replicate the gain curves. For this second model, additional adjustments were made to ensure that each curve started at 0 rather than centred around a common mean value.

3.3.3 2024 Testbeam Readout Data

To compare and verify which of the models was better, ToT readings were taken from a previous Testbeam in 2024. The values of 2.35ns at a threshold of 2.45 μA and 2.15ns at a threshold of 9.8 μA were recorded. These recordings were from the same channel from which the gain measurements were taken. The ToA-ToT plots for both of these readings are shown in [Figure 9] and [Figure 10], respectively.

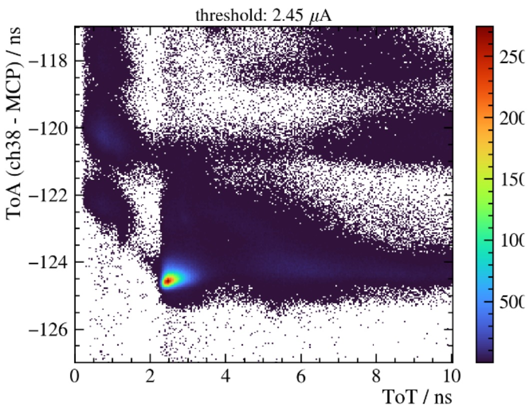

Figure 9: 2.45 μA Threshold

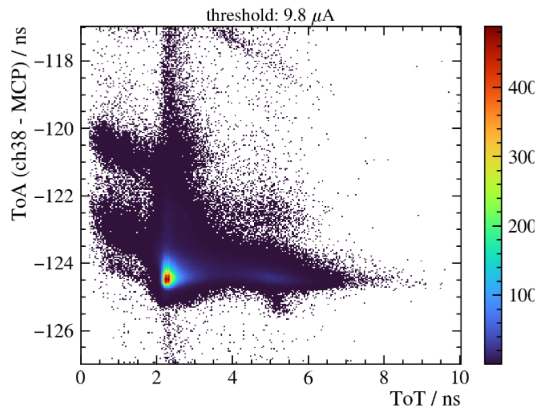

Figure 10: 9.8 μA Threshold

Figure 11: ToA vs ToT plots from previous 2024 Testbeam data at p-5 and p-20 threshold [31]

In the lab, a single pedestal value is 0.49 μA. Therefore, 2.45 μA and 9.8 μA refer to p-5 and p-20, respectively. From [Figure 11] it was obvious that most of the hits were located within a small area around their respective mean values, with the deep purple structures forming from a low density of hits. The vertical structures that are high in ToA and low in ToT were likely dark counts, which have thermal origins and can appear later than the expected signal [32]. The hits small in ToA but larger in ToT, causing the horizontal structures are probably noise. Both were unwanted effects and can be reduced by using higher threshold values. Therefore, the study focused on the high density core and its structure.

3.4 Simulating a Gas Chamber and Cryostat Testbeam

The primary aim of the design was to reduce the reconstructed Cherenkov angle resolution of the detected hits. Secondary to this was also the aim to reduce the size of the design so it can be kept as small and cheap as possible, as well as the aim to make a design which would work with different radiator materials, and hence was easily adjustable.

3.4.1 Benefits of a Gas Chamber and Cryostat

The cryostat will reduce the temperature of the SiPM to liquid Nitrogen temperatures ($77K$). Cooling the SiPM has multiple benefits, the first is that dark counts, thermally generated carriers, and noise is reduced at low temperatures. Additionally, the SiPM has better gain stability and reduced fluctuations improving efficiency [33].

The most obvious reason to use a gas chamber over a lens is the difference in refractive index, where a gas chamber's is much lower than the lens setup. A smaller refractive index will result in a Cherenkov ring with greater angular resolution, which will push the capabilities of the SiPM to limits similar to those of the actual RICH detectors and allowing the team to utilise the cooling effects of the SiPM.

3.4.2 Fixed Parameters and restrictions

When designing the new Testbeam setup for 2026, there were several restrictions and/or requirements set in place which would limit the flexibility of the designs. Importantly, the Cryostat was being designed in tandem with an engineering team and therefore was heavily restricted. This meant that the size of the cryostat, a cylindrical shape of radius 150 mm that was 600 mm long with a borosilicate glass window 10 mm thick and with a radius of 100 mm, was fixed. Moreover, the position, of the SiPMs within the Cryostat; placed 120 mm from the window into the cryostat, and occupying the corners of a square 110×110 mm^2, were also fixed. The material properties for the Borosilicate glass window had to be implemented, including absorption lengths and refractive indices [34]. These SiPMs had the same QE curves as outlined in Section (3.1.3). The initial dimensions of the chamber were set to $500 \times 500 \times 1000$ mm^3. As always, the beam line runs along the Z-axis with the structure of the setup rotating around this accordingly. Outside of the request to minimize the sizes of the apparatus, there was a lot of freedom when designing the gas chamber.

3.4.3 Proposed Setup Models

Several models and designs were investigated for this study, the first being a basic design where the photodetectors sat perpendicular to the beam, which moved through the gas chamber to create Cherenkov photons that would be reflected into the sensors. This model can be seen in [Figure 12], the mirror had a Radius of Curvature (ROC) of 3800 mm and the normal of the mirror was tilted 0.785 rad[1] with respect to the Z-axis.

Subsequently, after this initial design, the approach to angle the gas chamber box to the entering beam was also investigated, with both [Figure 13] and [Figure 14] using this method. The 'short angled beam' only differs slightly from the prior basic design, using a mirror with a ROC of 2100 mm and tilt of 0.570 rad; however, the gas chamber box was also rotated 0.448 rad relative to the Z-axis and beam. Similarly, the 'Long angled beam' also had the gas chamber box rotated, this time 1.244 rad with respect to the Z-axis. The ROC of the mirror increased to 2130 mm and was at a 0.174 rad tilt relative to the beam line.

Finally, the 'two mirror' setup, which uses both a spherical and a flat mirror. The ROC of the spherical mirror was 2100 mm and was tilted 0.08 rad from the Z-axis. The flat mirror was 164×120 mm^2 and tilted 0.865 rad with respect to the Z-axis. The centre of the flat mirror was placed 129 mm from the beam line. The gas chamber box had no rotation for this design.

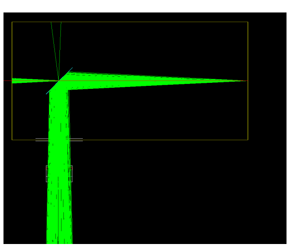

Figure 12: 'Basic' Cryostat setup

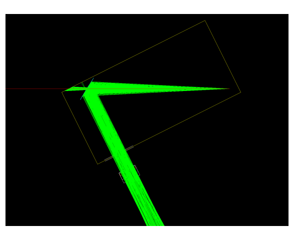

Figure 13: 'Short Angled' Testbeam

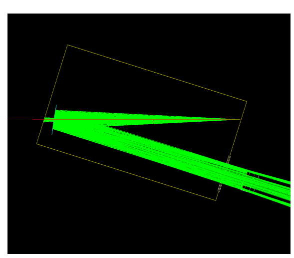

Figure 14: 'Long Angled' Testbeam

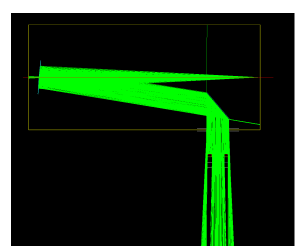

Figure 15: 'Two Mirror' setup

Figure 16: The geometric setups. The Z-axis aligned horizontally. Beam travels right to left.

[1]For this mirror and all subsequent mirrors, the rotation was clockwise when viewed from above and looking at the XZ plane, and the angle was between the Z-axis and the normal of the mirror

3.4.4 Two Mirror: Research and Development

The Models were put forward to a board that included the project supervisors, the head engineer, and the Testbeam project manager. During the meeting, the 4 initial designs were discussed, and the 'long angled' and the 'two mirror' setups were suggested. The head engineer explained how having the gas chamber box at an angle to the beam would make the 'long angled' setup much more awkward to use and showed favour to the 'two mirror' design instead. Following this, further development suggestions for that design were discussed.

Firstly, the 'two mirror' design could be improved by moving the flat mirror 113 mm past the beam so it was on the far side [Figure 17]. Because this increased the focal length between the circular mirror and the sensors, the gas chamber size was reduced to 900 mm, but the ROC of the curved mirror still increased to 2360 mm. Reducing the size of the gas chamber was one of the secondary objectives when designing. Therefore, this modification would be an improvement even if the resolution remained the same.

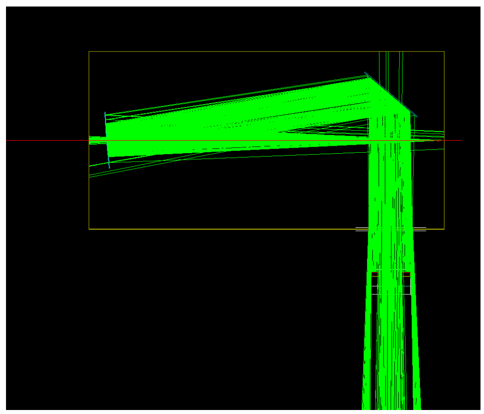

Figure 17: Two Mirror 'Opposite' setup with the flat mirror placed on the far side of the beam.

A secondary aim of these designs was to create a Testbeam setup that was easily adjustable. The easiest way to do this would be to align all the apparatus along the beam line [Figure 18]. Therefore, having a circular mirror with no tilt and ROC of 2320 mm while having the flat mirror sit in the beam line; reducing emission point error. Of course, to achieve this, the flat mirror had a hole cut into its centre, to allow the beam to pass through and stop secondary particles from disrupting the result. The hole had a 25.4 mm diameter.

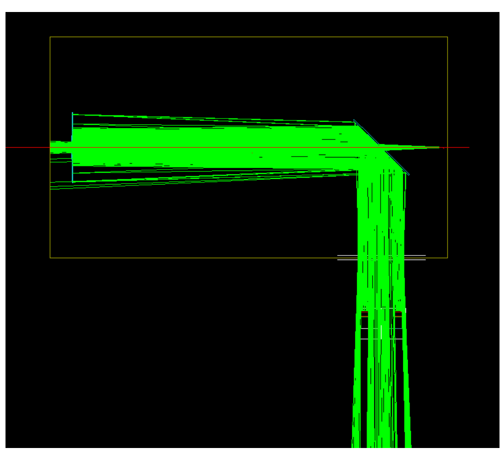

Figure 18: Two Mirror 'Aligned' setup with the flat mirror placed on the beam line.

Additionally, having all the mirrors aligned along the beam line meant that different gases could be investigated, to be used as radiators. Different gases would have different Cherenkov angles and therefore would require the mirror to be moved forwards or backwards. By installing a rail along the beam line axis (Z-axis), the mirror position could easily be adjusted. A lens in front of the Cryostat window would allow for focusing adjustments so that the photodetectors always sat within the focal plane.

With the introduction of lenses to focus the Cherenkov photons onto the sensor plane, the circular curved mirror could be removed altogether and replaced by a second flat mirror. Leaving the focusing entirely to the lens [Figure 19]. Both flat mirrors were $200 \times 200\ mm^2$, and meant that the photons would continue moving at the Cherenkov angle until the lens. The lens used was Bi-Convex and had an ROC of 450 mm and was 300 mm across. The advantage of this setup was that the gas chamber size can be drastically reduced to 700 mm in this case.

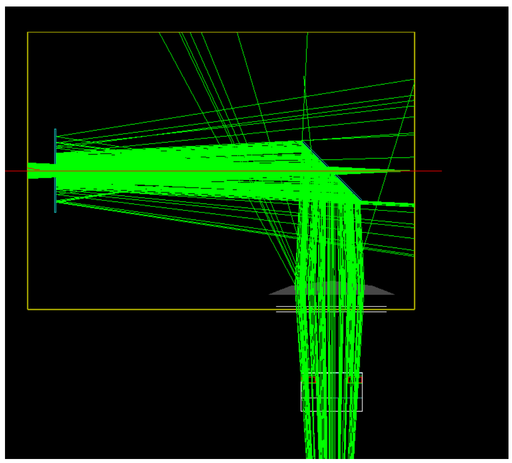

Figure 19: Two Mirror 'Lens' setup with two flat mirror and a lens used to focus the light on top the detectors instead of a circular mirror.

3.4.5 Additional Implications

Along side implementing Lenses to aid in the focusing of photons on the sensor plane, a beam width and beam divergence were added as options and explored to observe their impact. These types of beam modification should make the simulation more accurate to the real 2026 Testbeam, improving the data. Furthermore, alternative radiator materials, removing the 1-Hit protocol and Proton Synchrotron (PS) conditions, were investigated.

Beam width used a Gaussian spread to give the beam a probability of moving the starting position of the beam in the simulation. This moved the pencil beam so that over many events there was a simulated width.

Where as, beam divergence is the amount the beam is angled off the axis. With 0 divergence the beam line is always along the axis, this is the ideal condition; however, in experiment the beam line is not always exactly along the axis. Therefore, a divergence should be included in the simulation to mimic this effect. A Gaussian spread of angle in both the X and Y axes were sampled, the angles were then transformed into Cartesian directions which become the initial particles momenta values for X, Y and Z.

Being able to use alternative radiator materials and gases was one of the secondary goals to consider when designing the gas chamber. Therefore, the setup was tested using an alternative gas other than C_4F_{10}. To do this CF_4 was encoded in Geant4 and then placed inside the chamber instead. A range of refractive indices and absorption lengths were produced so that different wavelength photons were simulated correctly. This would also impact the Cherenkov production as the expected Cherenkov angle would shift from 0.051 rad to 0.033 rad [35].

The effect of turning of the 1-hit protocol was also investigated to see what impact this had.

Lastly, PS conditions run at much lower momentum relative to the Super Proton Synchrotron (SPS). Particles move at momenta such as 8 GeV instead of 180 GeV. Here, the Cherenkov radiation was no longer saturated, and PID may be possible as different particles could form different tracks. Assuming the design was unmodified under the PS conditions, observing the effect it had told if the design could be used in such environments.

Also mentioned was that occupancy along the ring arc could be as low as 35% without causing serious problems to the results. So this was set as the new marker and aim for any occupancy plots.

3.4.6 RICH Reconstruction

Reconstruction algorithms are used to accurately determine the Cherenkov angle of each hit, as well as the resolution of that Cherenkov angle. By utilising this reconstruction algorithm the resolution can be split into the three components and the amount that each one contributes can be calculated.

The algorithm works by using the fact that three unique points can create a plane. Therefore, by assuming the emission point of the Cherenkov photon as the mid point of the track, taking the centre location of the pixel that was hit, and the centre of curvature of the mirror, a plane can be formed. By using a fourth order equation, the location on the mirror where the particle reflects can be found. although the equation will have four results, two will be imaginary, and the third will be on the other side of the mirrors centre of curvature, leaving a single solution which will be the location that the particle reflects off the mirror. Knowing the point in which it hits the mirror, and assuming the start location as the mid point, trigonometry can be used to calculate the Cherenkov angle.

To determine how much each error affects the resolution, certain characteristics in the reconstruction are changed. For pixel error, the specific hit location is taken instead of the centre of the pixel, then the reconstruction is completed the same as before. The difference in the resolution is because of pixel error. Then using the simulation, the exact location of Cherenkov photon emission can be used instead of estimating and using the tracks mid point. Again the reconstruction is repeated and the difference in resolution is due to the emission point error. This assumes that the sensors are in the focal plane of the mirror. Finally, by applying both of these changes at the same time, the resolution can only be a contribution of the chromatic error.

Ideally, each of the individual errors resolutions should be minimised but, more importantly, equal. If none of the errors dominate the other two, then the setup is in its ideal state.

4 Results and Discussion

The Results follow the methodology sections laid out throughout section (3).

4.1 Results from the 2025 Testbeam Study

Within the first study, where the October 2025 Testbeam setup was simulated, the QE curves of the different photomultipliers are plotted and compared. Two types of occupancy plots are then made and observed to understand and justify if SiPMs are a suitable upgrade over the current MaPMTs.

4.1.1 Quantum Efficiency Curves of Different Photodetectors

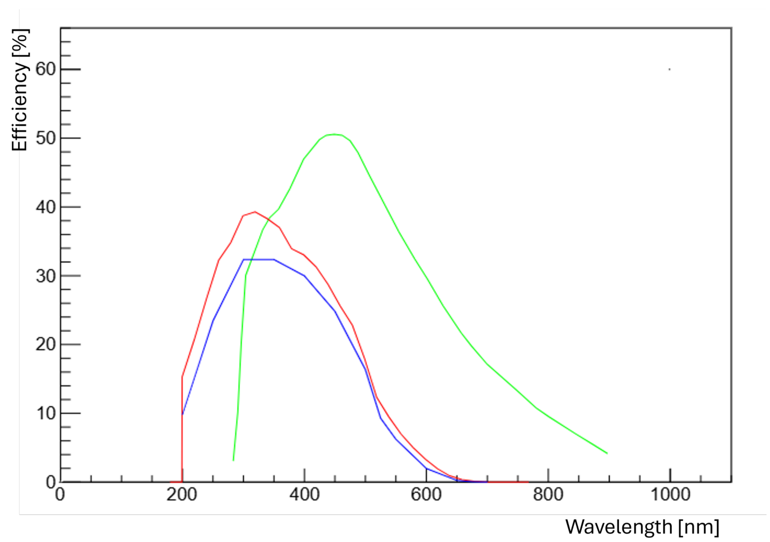

Figure 20: Quantum Efficiency against wavelength curves for 1-inch MaPMT (red), 2-inch MaPMT (blue) and SiPM (green) [36].

As expected, the 2 MaPMTs have very similar QE curves, with the 1-inch detector having a slight increase in efficiency especially around the $300nm$ range, while the SiPM curve was larger and shifted to longer wavelengths.

In fact, the SiPM curve started at $300nm$ cutting off all photons with smaller wavelengths, This was not a problem, however, as from [Figure 6] it was obvious that the photon production was from $300+$ nm and therefore the MaPMTs have an increased inefficiency in the setup as much of their efficiency was below this 300 nm boundary. Returning to the SiPM, [Figure 20] also demonstrated the superior efficiency of the SiPM detector, which had a peak efficiency of $\sim 54\%$ at 450 nm compared to $\sim 40\%$ and $\sim 32\%$ for 1-inch and 2-inch MaPMTs, respectively. Furthermore, the MaPMTs stopped around 650 nm whilst the SiPM continued until 900 nm which again was significant, as identified earlier, the majority of photons created by the Cherenkov radiation were within the $300 - 900$ nm range. A photodetector that can capture that entire range would be better suited for the RICH detector as it would not miss out on any crucial data. These QE curves were the first insight into why the SiPM would be a good replacement for the MaPMTs.

4.1.2 Occupancy of the Setup

To understand the simulation data, many types of plots were created, and an important plot for spatial data is a pixel occupancy plot. The aim of a pixel occupancy plot is to show what the probability of a photon hitting each pixel within an event would be. The pixel occupancy plot for the 2025 Testbeam simulation is below;

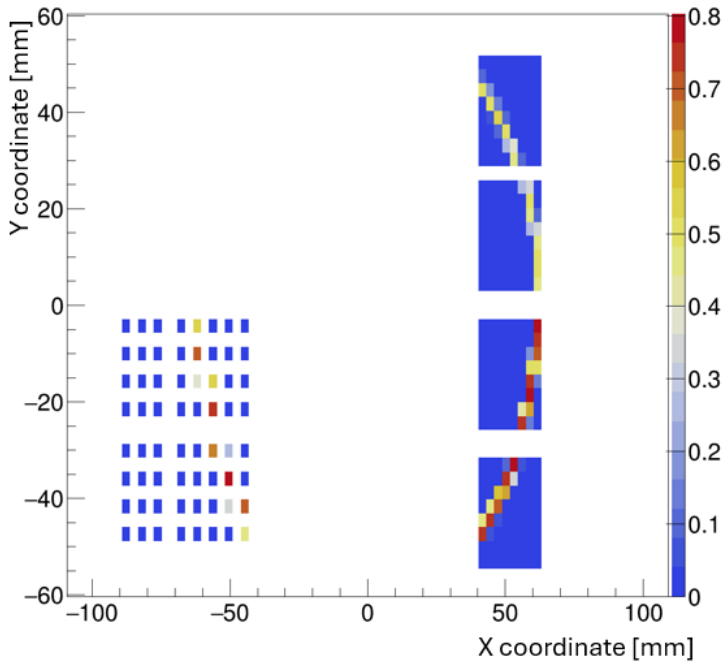

Figure 21: 2D histogram plot of the Pixel occupancy over 10,000 events.
The colour scale indicates the percentage chance a pixel detects a photon in a single event.
2-inch MaPMT (bottom left), 1-inch MaPMT (top right two), SiPM (bottom right two).

From [Figure 21] the 2-inch MaPMT and SiPM had much higher average occupancy at $\sim 70\%$ and 75% respectively, while the 1-inch MaPMT was lower at $\sim 50\%$, along the arc of the Cherenkov ring. These occupancies were much larger than those observed in LHCb-RICH, where occupancy is limited to $< 30\%$ [37]. However, occupancy is closely related to the optical geometry setup of a system. The October 2025 Testbeam geometry is aimed at testing the photodetectors in the setup, this means there are more hits per pixel in the 2025 Testbeam configuration when compared to the current RICH, and therefore occupancies of 2-3x are not surprising to see and are expected for this simulation.

Although the SiPM and 2-inch MaPMT had relative occupancies of 75% and $\sim 70\%$, the two types were not equally good candidates in this setup. This was because the pixel size of the 2-inch MaPMT was $4\times$ larger than that of the SiPM and 1-inch MaPMT, which explains the increased occupancy of the 2-inch MaPMT. Furthermore, using (equation 7) and knowing that the focal length was equal for each detector in this setup, the pixel error was then only dependent on the pixel size. Therefore, the 2-inch MaPMT had a pixel error $4\times$ larger than the other two photodetectors.

$$\sigma_{pix} \approx \frac{P}{f} \tag{7}$$

σ_{pix} is the pixel error, P, is the pixel width and f is the focal length.

This data was recast as occupancy per pixel for each type of photodetector individually. Doing this highlighted the average occupancy for each detector more clearly and allowed for a better measurement of it. The 1D occupancy plots also showed how only pixels along the Cherenkov ring arc get consistent hits, as pixels not along this arc have almost no occupancy. The knowledge of which pixels were on the ring arc and which were not allows for finer tuning of the Testbeam setup. This allows the position of the detectors to be adjusted so that they are in optimum places that cover the most ring, and where the most pixels are activated.

Looking at the 2-inch MaPMT plot in [Figure 22] it also exaggerates the point made previously about how this photomultiplier had less spatial accuracy with few pixels contributing to the detector occupancy. This was because it only had 64 pixels, whereas the other two detectors, seen in [Figure 23] and [Figure 24], had 128 pixels spread over two separate sensors. The fact that there were two detectors also allows for finer tuning and positioning to maximise Cherenkov ring coverage without having additional wasted space.

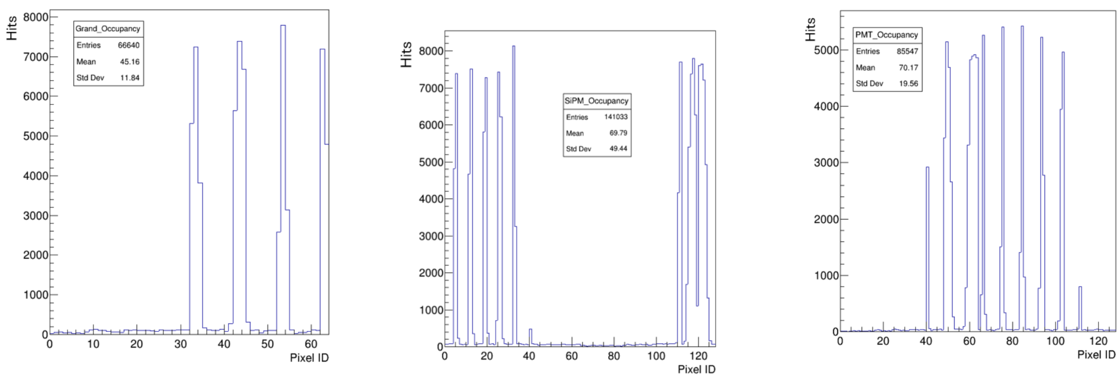

(a) (b) (c)

Figure 25: 1D occupancy plots showing the percentage occupancy for the pixel ID per detector: a) 2-inch MaPMT, b) SiPM, c) 1-inch MaPMT.
For b) and c) the first 64 ID numbers are for the lower detector whilst the latter 64 are for the higher detector in the Y plane.

These results from the 2025 Testbeam simulation show that the SiPM would be a better candidate for RICH than the MaPMTs due to the increased occupancy. However, upgrade II requires the chosen detectors to also have a significant work rate and be reliable in high luminosity environments, such as the HL-LHC, which this study has not shown. Compared to current $3 \times 3\ mm^2$ pixels, a pixel size of $1\ mm^2$ would be more ideal. However, this would drastically increase the number of channels and therefore the cost would also significantly spike.

4.2 Comparing 25-713 Lens to 25-709 Lens

One Benefit of using a larger lens was that it created a larger Cherenkov ring which meant electronic components were moved further away from the beam line. When using the 150 mm lens, as seen in [Figure 21], the centre of the photodetectors were ~ 50 mm from the beam. When using a 200 mm lens, the detectors can be moved to between $75 - 85$ mm from the beam, as seen in [Figure 26].

4.2.1 Comparing Occupancies

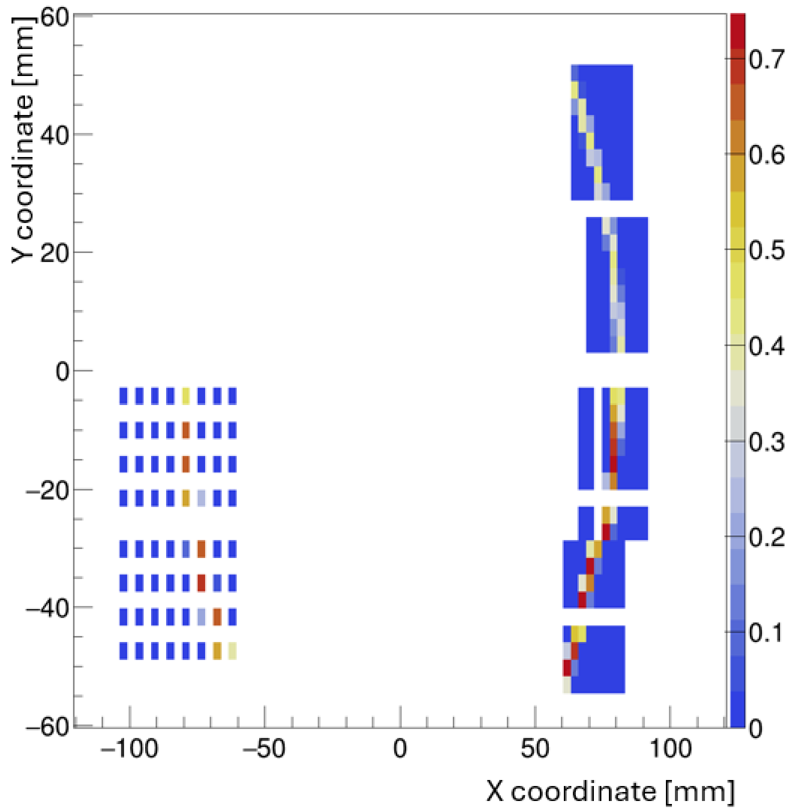

Figure 26: 2D histogram plot of the pixel Occupancy of the 27-513 200 mm lens. The 2-inch MaPMT, top 1-inch MaPMT and bottom SiPM have been moved 20 mm further from the beam line, whilst the bottom 1-inch MaPMT and top SiPM have been moved 25 mm further from the beam line.

When the larger lens was used, the occupancy of all three detectors decreased by $\sim 14\%$. The SiPM, 1-inch, and 2-inch photodetectors have occupancies of 70%, 40% and $\sim 60\%$ respectively. Most likely caused by an emission-point error where the larger lens had a greater focal length. Because of the relatively fixed position of the detectors, they may have sat outside the focal plane of the lens causing this decrease in occupancy. Interestingly, the number of detected hits per event remained relatively similar between the two lenses, going from 29 Hits Per Event (hpe) with the 27-509 lens, to 28 hpe with the 27-513 lens. So, this decrease in occupancy could also be because there were more pixels along the larger ring arc for the same number of photons. This would cause a drop in the occupancy percentage.

4.2.2 Comparing Cherenkov Angle Resolution

Another way the lenses were compared to validate which was better to use in the setup, was by reconstructing the Cherenkov angle of the detected photon hits in the sensors.

$$r = \frac{R}{2} tan(\theta) \tag{8}$$

rearranged to get,

$$\theta = atan\left(\frac{2r}{R}\right), \tag{9}$$

here, θ is the Cherenkov angle, r is the radius of the ring formed on the sensors, whilst R is the radius of curvature of the mirror used.

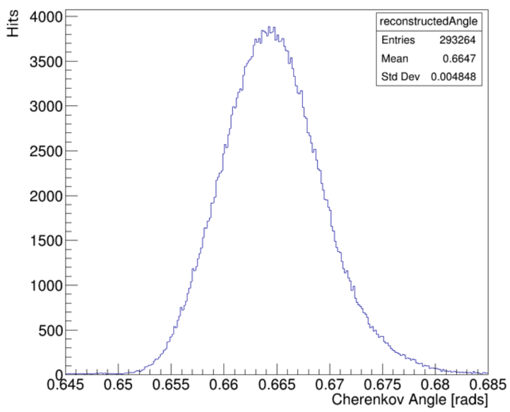

(a)

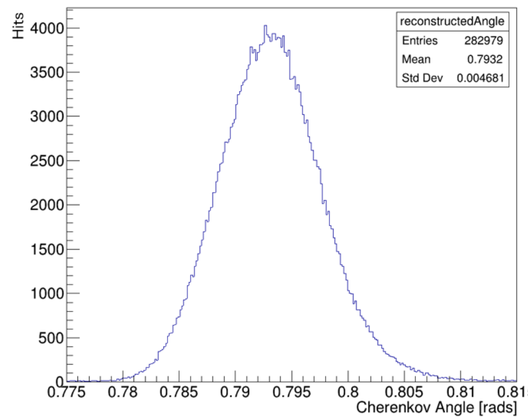

(b)

Figure 29: Simple Cherenkov angle reconstruction of each detected hit within the simulated setup, a)left 27-509 lens b) 27-513 lens.

A smaller Cherenkov angle resolution implies a better geometric setup. [Figure 29] showed that the 27-509 lens had a resolution of 4.85 mrad. However, the 27-513 lens had a better resolution of 4.68 mrad. In contrast to the occupancy plot, the resolution was better for the larger 200 mm lens by 0.17 mrad. This difference was quite small, with only a 4% improvement over the current lens. Unfortunately, without using the full reconstruction algorithm described in section (3.4.6), there was no way of knowing how much each of the three individual resolutions makes up this total resolution. Also notice that the mean values in the plots above differ slightly from each other. This inaccuracy was caused by using (equation 9), which was an estimation of the optical geometry of the setup. However, this had negligible impact on the resolution of the reconstruction and therefore was not a big concern, but rather something that should be noted.

Provided with both the occupancy plot in [Figure 26] and the reconstructed angle plot in [Figure 29], there was little difference between the results of the two lenses. Given that the 150 mm lens had been used in previous Testbeams, it was recommended to stay with this option, as the results are not significant enough to justify spending funding on a new lens.

4.2.3 Beam Width Result

When a 5 mm beam width was added to the simulation, negligible differences were observed; occupancy remains the same while the angular resolution increases by $\sim 1\%$. Therefore, a beam width did not cause any problems in the 2025 Testbeam.

4.3 Simulated Readout and Timing Data

This section demonstrates the effects of the SiPM and FastRICH on the timing data, specifically, the effect they have on the time walk.

4.3.1 Which of the Models was Better

When comparing the Difference-of-exponentials and Gaussian models, not only was the Gaussian curve easier to implement, allowing better understanding and fine-tuning of the model, but it also gave more reliable results that were more accurate to the values recovered from the previous Testbeam data. The Gaussian model got mean times of 2.31 ns and 2.10 ns at 2.45 μA and 9.8 μA thresholds, respectively. The exponential model had 2.08 ns and 1.20 ns for the same thresholds. Recall from section (3.3.3) that the 2024 Testbeam produced measurements of 2.35 ns and 2.15 ns, respectively, for these thresholds. Clearly, the Gaussian model was a better fit for the simulation with an average error of 45 ps compared to the error of the exponential model of $\sim$ 580 ps. Given this, the Gaussian model was chosen for any further use in the simulation.

4.3.2 Investigating ToA vs ToT plots

The plots in [Figure 11], did not have any visible time walk, which was unexpected. The team working on the Testbeam believed that this was due to the hardware improvements making it negligible at thresholds so close to the pedestal, which are just fractions of the maximum amplitude of the gain curves. In response, the lab tested the channel with increasing thresholds to try and determine if this theory was right, and if so, at what threshold would time walk be observed.

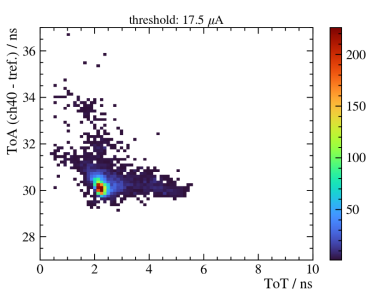

Figure 30: 17.5 μA Threshold

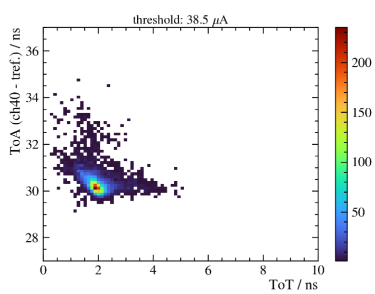

Figure 31: 38.5 μA Threshold

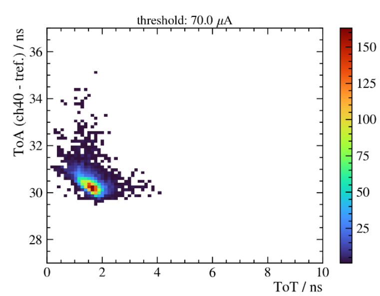

Figure 32: 70 μA Threshold

Figure 33: ToA vs ToT plots using measured values from the CERN lab

As shown in [Figure 30], the time walk was first visible around $\sim$ 17.5 μA and the effect became clearer, the higher the threshold was. As expected, the number of low density structures reduced with increasing threshold. A higher threshold meant that fewer hits passed the threshold amount and did not trigger the readout. Due to this, each plot in [Figure 33] had a decreasing number of total hits and a decreasing scale, which would increase any error within the plots. These laboratory-made plots could also be used to further validate the readout simulation model. Having more ToA-ToT plots to compare between means that the model could be better justified.

Given the aim was to calculate the mean ToT and find the time walk within the system, the low density structures could be ignored. Since neither dark counts nor noise were added to the simulation, only the high density structure within [Figure11] were created and seen in the plots below.

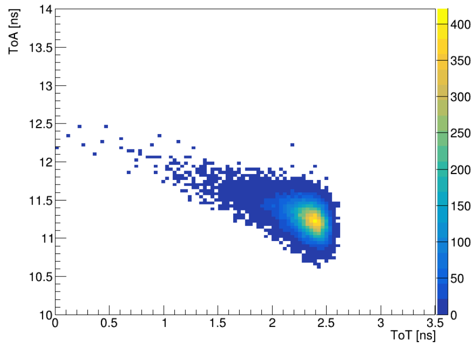

Figure 34: 2.45 μA Threshold

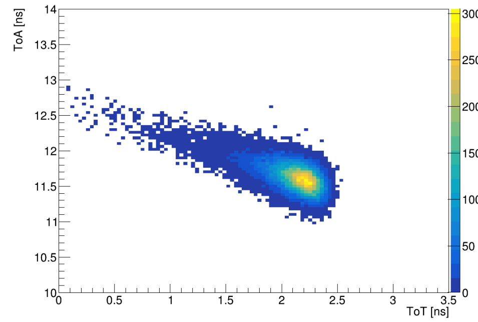

Figure 35: 9.8 μA Threshold

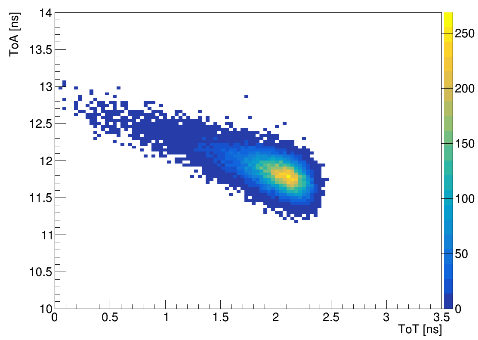

Figure 36: 17.5 μA Threshold

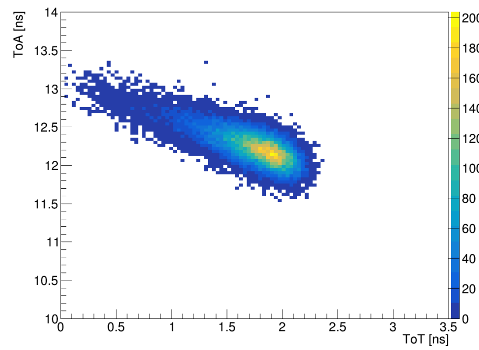

Figure 37: 38.5 μA Threshold

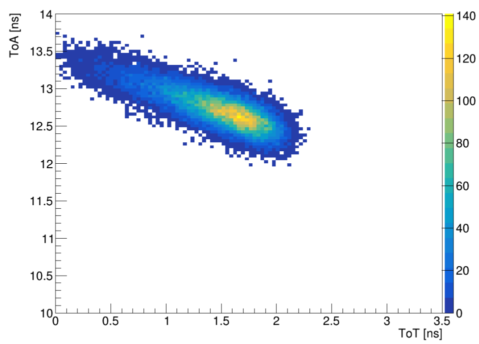

Figure 38: 70 μA Threshold

Figure 39: ToA vs ToT plots created using the Gaussian model within the simulation. each hit detected had a ToA and ToT value calculated and then put in to 35 ps timing bins.

The plots within [Figure 39], had a high hit count core (seen in yellow) with a trailing low hit count tail. This tail indicated a level of time walk even at lower thresholds, although this time walk was negligible until around 17.5 μA. The tail was visible in the simulated plots as they did not have the low density structures.

[Figure 36], [Figure 37] and [Figure 38], could be compared to the lab-created plots in [Figure 33]. The simulated data recreated these plots well, reflecting the shape of the core within each respective plot. As the threshold increased, the shape of the plot became more elongated and also shifts to a smaller ToT, with an average value of 1.96 ns, 1.71 ns and 1.45 ns respectively. All of these had an error of < 100 ps relative to their matching plot. The more stretched a plot was, the greater the time walk and the larger the error between different gain curves. There was a time walk of 350 ps, 400 ps and 550 ps for the 17.5 μA, 38.5 μA and 70 μA thresholds, respectively. Knowing the amount of time walk allows the chip to make adjustments for the given gain curves to reduce and eliminate the effects of time walk.

Given the agreement with previous Testbeam data and laboratory data, the Simulated Gaussian model can be used to create accurate timing data within an error of $\pm 100\ ps$. This data can then be used to account for time walk within the Testbeam, meaning tighter time cuts can be made reducing noise.

4.4 Results and discussion of Cryostat and Gas Chamber Investigation

This section covers the April 2026 Testbeam simulation. The results were used to suggest the optimal design for the gas chamber to the Testbeam team. The study was important because the construction of the cryostat and gas chamber is based on the final design. Furthermore, depending on the success of the study, the design could be used beyond the April 2026 Testbeam and in other future projects.

4.4.1 Model comparisons

This study used occupancy and angular resolutions as the main way to compare and determine the best designs and setups. Therefore to do this all plots are of the same scale so that they are easy to compare to one another. Some additional factors, such as engineering feasibility, can also impact certain decisions.

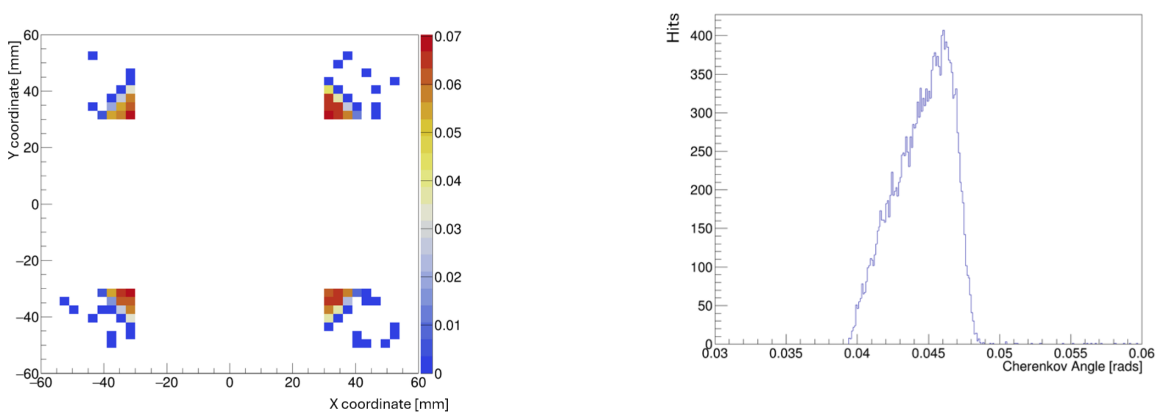

(a) (b)

Figure 42: Plots for the 'Basic' design. a) Pixel occupancy plot indicating the percentage chance each pixel detects a hit in a given event. b) Cherenkov angle Plot showing the reconstructed angle of each hit detected.

The 'Basic' setup created a poor result, as seen in [Figure 42], the Cherenkov ring produced was too small for the SiPM setup within the cryostat. Increasing the mirror size to accommodate this issue increased the focal length of the mirror far past the position of the SiPMs. These problems resulted in a reconstructed Cherenkov angle with a resolution of 2.01 mrad. for reference The current RICH detectors have an overall resolution of 0.8 mrad [38].

To improve this design and try to avoid the same problems, [Figure 13], the 'Short Angled' model was created. The idea was that by angling the box and moving the mirror further back, the photon ring reflecting on the mirror would be larger. This meant a smaller mirror could be used, and it would have a focal length closer to the position of the SiPMs.

However, the occupancy plot in [Figure 45] clearly showed that this design had the same problems as the previous design, with these designs having a max arc occupancy of $\sim 7\%$ and $\sim 11\%$, respectively. The Cherenkov ring was too small for the position of the SiPMs and yet making the ring larger caused the resolution to increase drastically. The issue was that the distance between the mirror and the photodetectors needed to be severely increased. Similarly to the Basic setup, the resolution of the Cherenkov angle was poor, and with 1.60 mrad, this was a magnitude of scale to large.

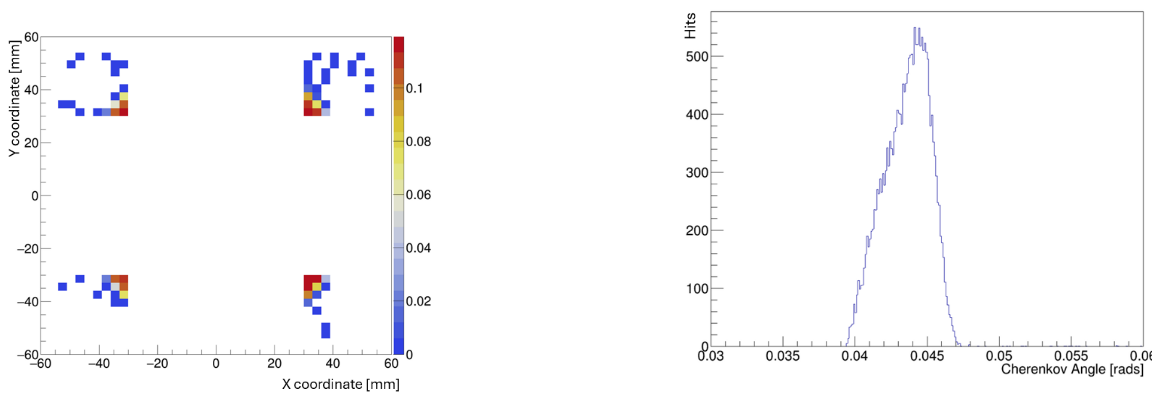

(a) (b)

Figure 45: Plots for the 'Short Angled' design. a) Pixel occupancy plot indicating the percentage chance each pixel detects a hit in a given event. b) Cherenkov angle Plot showing the reconstructed angle of each hit detected.

This time, to fix the issues in the previous designs, the focus was to increase the distance between the mirror and the sensors. The solution; rotate the gas chamber box 90° so that the long side was parallel to the cryostat, as seen in [Figure 14]. To ensure that the track remained in the chamber for sufficient time, the entire setup was also angled to the beam. This means that the photons can travel at the Cherenkov angle long enough to create a ring large enough to form on the SiPMs. The ideal ring radius for the given fixed parameters was 63 mm.

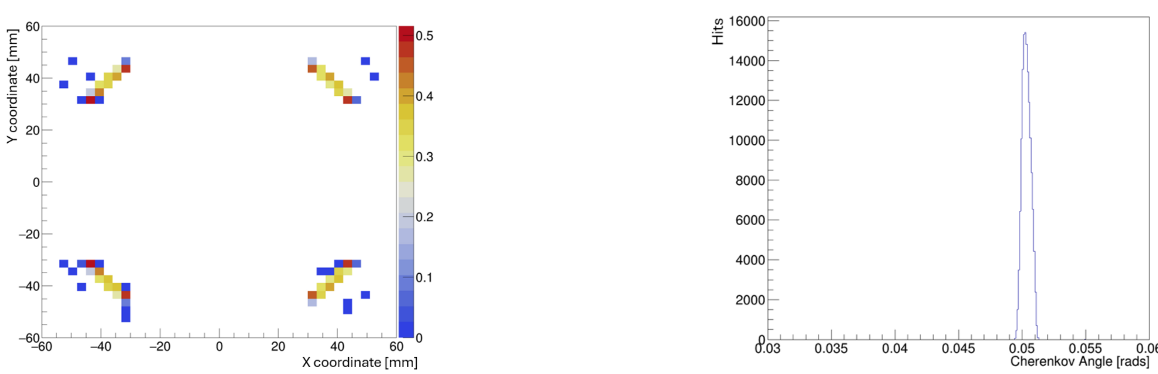

(a) (b)

Figure 48: Plots for the 'Long Angled' design. a) Pixel occupancy plot indicating the percentage chance each pixel detects a hit in a given event. b) Cherenkov angle Plot showing the reconstructed angle of each hit detected.

These modifications were successful and the changes meant that the Cherenkov ring had a radius large enough to form on the SiPM detectors, clearly seen in [Figure 48]. This results in an average occupancy of 35% along the ring arc. The focal plane of the mirror used aligns with the detectors position in the cryostat. The result of this was a Cherenkov angular resolution of only 0.34 mrad. This angular resolution was over 4× smaller than that of the 'Short Angled' design. Furthermore, this was a reduction of 57.5% to the current RICH models.

The last of the initial designs that were investigated used two mirrors instead of only one. This meant that the chamber would not need to be rotated at all, and could remain perpendicular to the cryostat as well as parallel to the beam.

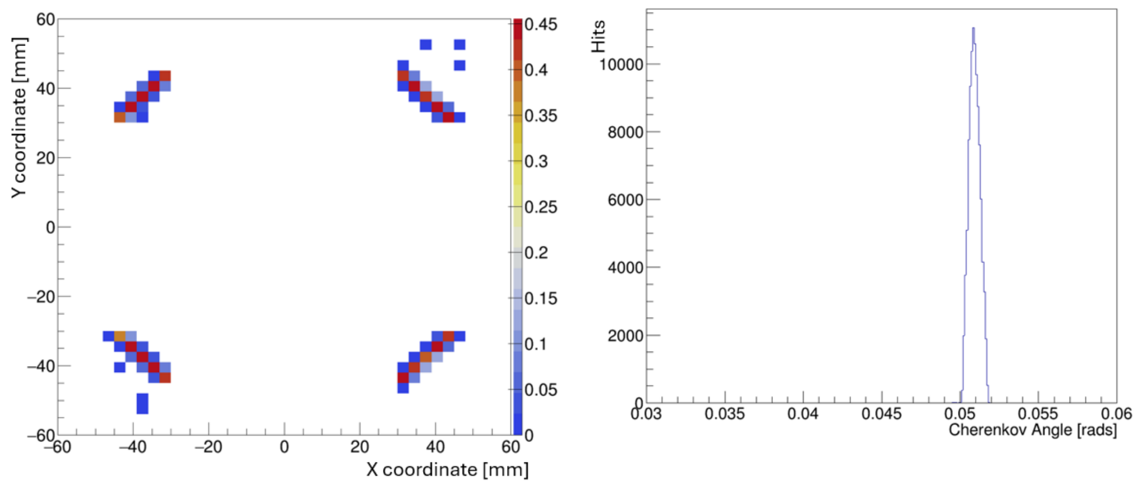

(a) (b)

Figure 51: Plots for the 'Two Mirror' design. a) Pixel occupancy plot indicating the percentage chance each pixel detects a hit in a given event. b) Cherenkov angle Plot showing the reconstructed angle of each hit detected.

The addition of a second mirror made the positioning of the setup much easier. With two mirrors, getting the SiPMs to align with the focal plane of the curved mirror was less challenging. The downside of having a second mirror was that you had a slightly lower yield of hits, this was because each mirror was not a perfect reflector and lost $\sim 11.7\%$ of photons. Because of this loss in photons, the hits per event go from 16 hpe for the 'Long Angled' design down to ~ 8 hpe for this 'Two Mirror' setup. Despite this, the occupancy actually increased to 45%, which was an average +10% per pixel along the ring arc relative to the 'Long Angled' setup. Finally, the Cherenkov angle resolution of the two designs was very similar as well, with the 'Two mirror' having a resolution of 0.342 mrad; only 2 μrad larger than the 'Long Angled' which was a negligible difference.

After discussing with the head engineer, the Testbeam project manager and the project supervisor, The 'Two Mirror' setup was favoured, and further research into this design was suggested. This was because of the relative angular resolutions between the two latter designs as well as the significant improvement to the occupancy of the 'Two Mirror' setup. However, the final reason why this model was preferred by the board was because of the easier mechanical logistics, compared to the 'Long Angled' setup, which, due to its angled box and mirror tilts, had more chance for errors.

4.4.2 Further Study into the Two Mirror Setup

By moving the flat mirror to the far side of the testbeam, the size of the gas chamber was reduced to 90% of the original design size. The major issue with this design was that the ring occupancy dropped to $\sim 25\%$. This was -10% lower than the new agreed upon limit; 35%. Unlike occupancy, the resolution had improved using this design, with a Cherenkov angle resolution of 0.301 mrad. This was the greatest reduction in the Cherenkov angle resolution of any design and was likely because this design had the spherical mirror with the largest ROC which would reduce spherical aberration, therefore reducing emission point error [39]. Additionally, the larger mirror had a larger focal length, and from (equation 7) this meant that the setup would have had a smaller pixel error too.

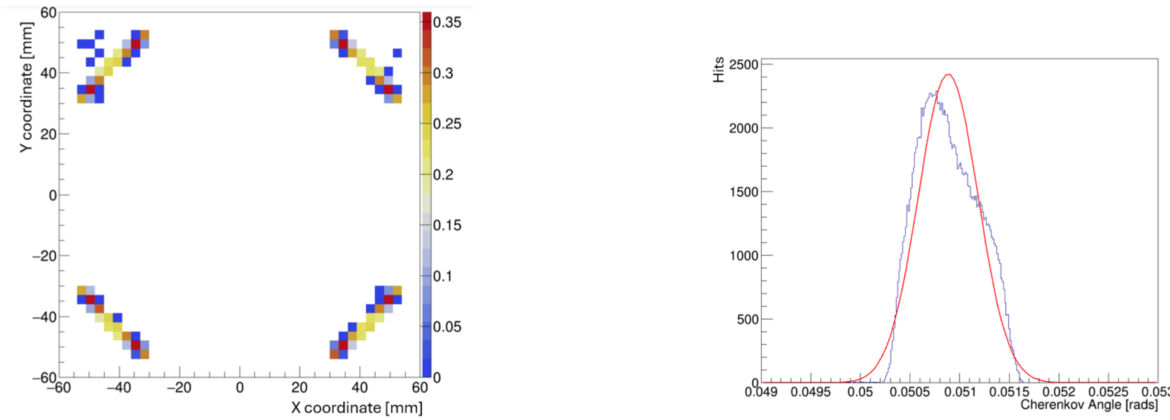

(a) (b)

Figure 54: Plots for the 'Opposite' design. a) Pixel occupancy plot indicating the percentage chance each pixel detects a hit in a given event. b) Cherenkov angle Plot showing the reconstructed angle of each hit detected.

Interestingly there were 8 pixels in the occupancy plot for the 'Opposite' design, [Figure 54] which had a suspiciously high occupancy. This was due to the specific size of the ring and the positioning of the detectors misaligning slightly, and therefore, these pixels got more photons than surrounding pixels. This created a false occupancy of 35% for these 8 pixels. To show that this was was happened and that there was no odd photon clumping, [Figure 55] shows the hits recorded in the detectors without any pixels. In this plot, the photons are clearly uniform along the ring arc.

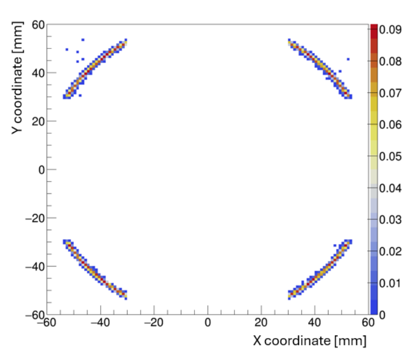

Figure 55: Hit occupancy plot (no pixels) for 'Opposite' setup

Next, the 'Aligned' design was tested and shown in [Figure 58]. This design was a good balance between the two prior designs. With an occupancy of 35%, this design was better than the 'opposite' setup but worse than the 'Two Mirror' model. Where as the Cherenkov angular resolution, at 3.15 mrad, was better than the 'Two Mirror' setup but worse than the 'Opposite' setup. The Advantage of this design was that all the mirror components were aligned along the beam line. This made the placement of all the components easier and reduces the emission point error as the curved mirror had no tilt, hence a better resolution than the 'Two Mirror' design. This design was also best when using different radiator materials as only the position of the curved mirror needed to be change instead of the whole setup.

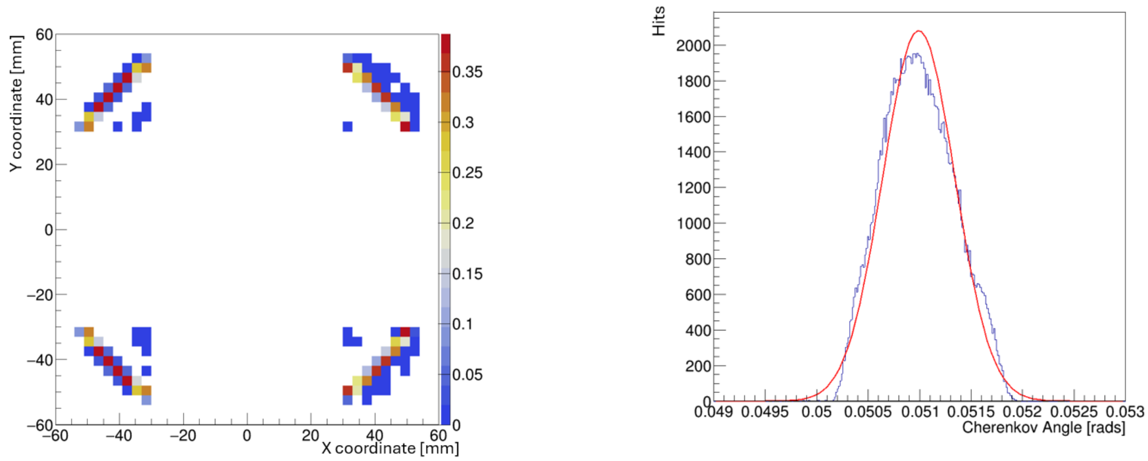

(a) (b)

Figure 58: Plots for the 'Aligned' design. a) Pixel occupancy plot indicating the percentage chance each pixel detects a hit in a given event. b) Cherenkov angle Plot showing the reconstructed angle of each hit detected.

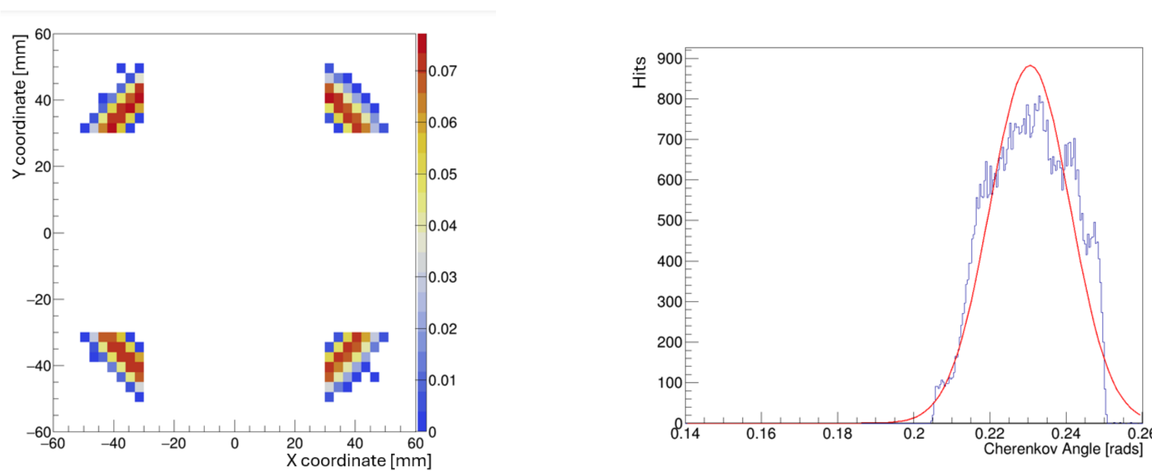

(a) (b)

Figure 61: Plots for the 'Lens' design. a) Pixel occupancy plot indicating the percentage chance each pixel detects a hit in a given event. b) Cherenkov angle Plot showing the reconstructed angle of each hit detected.

Finally, the setup with a lens was simulated. The occupancy using this design drops to 7%, as seen in [Figure 61], this was too small to be considered as a candidate. Similarly, the Cherenkov angular resolution increases by two magnitudes of orders, to 10.5 mrad. The issue with the lens model was seen through (equation 11); the radius of the Cherenkov ring required for the position of the SiPMs was $\sim 63\ mm$ and with C_4F_{10} the Cherenkov angle was 0.051 rad, meaning the focal length required for the lens to focus the ring onto the detectors was $1224\ mm$. Using (equation 13), the distance between the lens and the sensors would need to be greater than that focal length. This would mean that the lens would sit between the two flat mirrors and the chamber would need to remain $1000\ mm$ instead of being $700\ mm$. This defeats the whole point of using two flat mirrors and a lens, and therefore this design was a fail and the curved mirror setups were better.

$$f = \frac{R}{2(n-1)} \tag{10}$$

$$r = f\tan(\theta) \tag{11}$$

$$r = \frac{R}{2(n-1)}\tan(\theta) \text{ or } R = \frac{2r(n-1)}{\tan(\theta)} \tag{12}$$

$$\frac{1}{f} = \frac{1}{d_{obj}} + \frac{1}{d_{img}} \tag{13}$$

The plots in this section have also been fitted using a binned likelihood (in red). The fit was a Gaussian distribution based on the simulations results. The sigma was determined by the Cherenkov angular resolution measurement.

4.4.3 Beam Width and Beam Divergence Results

The 2026 Testbeam is capable of ensuring a beam width between $5-10\ mm$ with an average of $\sim 6\ mm$. Therefore, in the simulation, a beam width of $6\ mm$ was tested to see what its impact on the data was. With the realistic beam width added, there was no change to the occupancy or angular resolution for the 'Aligned' setup, which was used as the base design.

Larger beam widths were also tested and observed in [Figure 65]. There began to be an artifact forming on the flat mirror within the aligned setup. This artifact was a vertical line of hits that appeared on the mirror and worsened with increasing beam width.

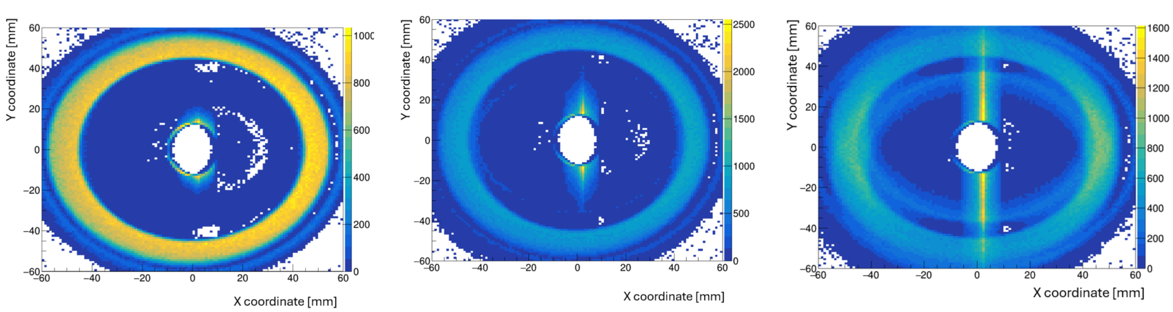

(a) (b) (c)

Figure 65: Detected hits on the flat mirror of the 'Aligned' design when the beam width was increased to a)12 mm, b)24 mm and c)60 mm wide.

As well as beam width, beam divergence was also created. This differs slightly because beam divergence changed the angle of the incoming beam, not the position. The beam divergence was tested at 4 different divergence angles; 2.5, 5, 10, and 25 mrad.

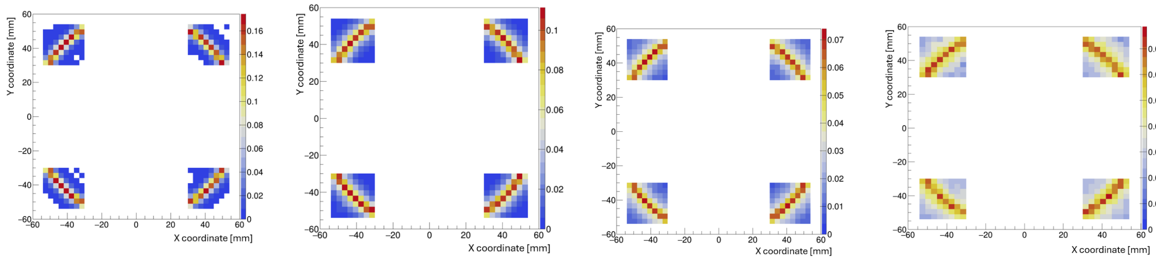

(a) (b) (c) (d)

Figure 70: Pixel occupancy plots indicating the percentage chance each pixel detects a photon in a given event for simulations with a beam divergence added.
a) 2.5 mrad, b) 5 mrad, c) 10 mrad, d) 25 mrad.
Based off the 'Aligned' setup from [Figure 58].

As expected, the more the beam was allowed to diverge, the greater the effect on the end results. With occupancy along the ring arc as 16%, 10%, $\sim$ 7% and $\sim$ 3%, for the different divergences, respectively. Even with low divergence there was still a large drop in occupancy, and this could cause data collection problems.

The smearing effect was also visible when looking at the resolution graphs in [Figure 75]. The resolution peak widens proportionally with the divergence.

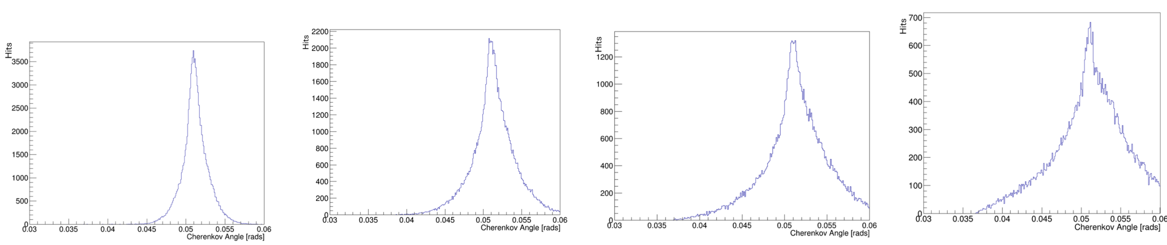

(a) (b) (c) (d)

Figure 75: Resolution plots for simulations with a beam divergence added.
a) 2.5 mrad, b) 5 mrad, c) 10 mrad, d) 25 mrad.
Based off the 'Aligned' setup from [Figure 58].

Even with a small beam divergence of 2.5 mrad, the Cherenkov angle resolution increased nearly 5$\times$ to 1.70 mrad. At 5 milliradians it had a resolution of 2.84 mrad and reached a resolution of 3.78 mrad and 4.46 mrad when there was a deviation of 10 and 25 mrad, respectively.

The results of this investigation were interesting because even at the lowest divergence tested, the impact on the results was significant and would affect the Testbeam data. This was unlike the beam width, which had negligible impact. Because of this study, the Team now knows to focus on reducing and preventing beam divergence in the Testbeam.

4.4.4 Testing different Radiator Gases

One of the secondary goals in the design of the gas chamber was to create a design that could use alternative radiator materials. Therefore, an alternative radiator material was used in the simulation to measure the effects it had. For this CF_4 was tested, which had a lower refractive index than C_4F_{10} and therefore had a smaller Cherenkov angle.

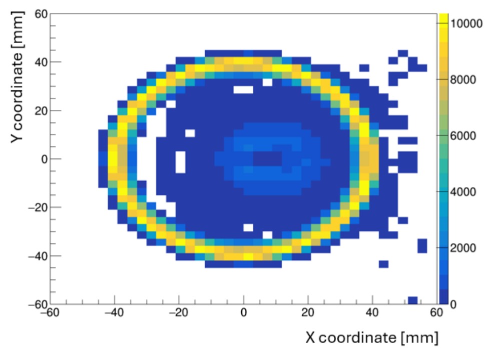

Figure 76: Photon XY position in the photodetector plane. The Cherenkov ring had a radius of 39 mm.

When the setup was kept as the 'Aligned' design, a good ring formed in the detector plane as seen from [Figure76]. The resolution of the ring should be similar to that of C_4F_{10} gas. However, this Cherenkov ring only had a radius of 39 mm, which was too small to land on the detectors given their position in the cryostat. Because the SiPM position were fixed, CF_4 cannot simply be switched in without changing the design.

It was still possible to obtain a ring that formed on the detectors with a good angular resolution of 0.873 mrad, however, the occupancy dropped to $\sim 12\%$, which was significantly lower than the 35% marker set. The large issue with this design change was that it requires the gas chamber to be made longer, to a length of 1700 mm, which was an increase of 70%. This increase in size ignored the secondary aim of reducing the size. This was due to the change in the refractive index causing a smaller Cherenkov angle of 0.033 rad.

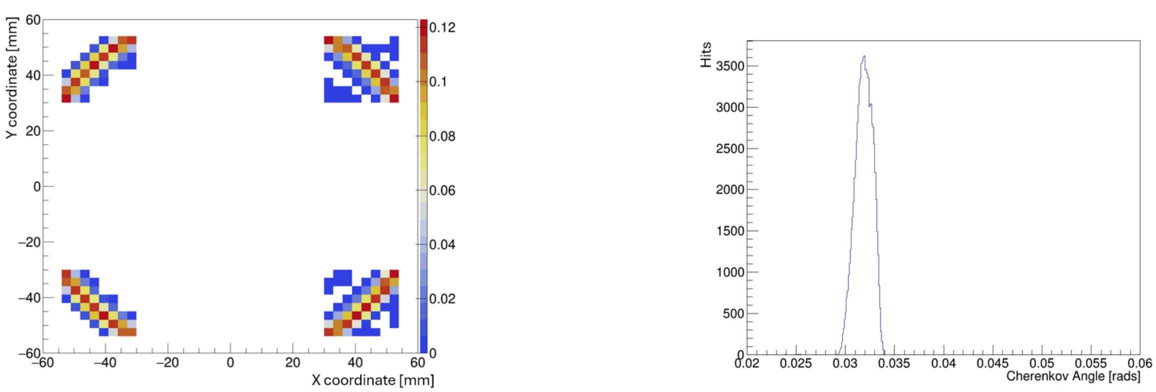

(a) (b)

Figure 79: Plots for the 'Aligned' design but CF_4 is used as the radiator gas. a) Pixel occupancy plot indicating the percentage chance each pixel detects a hit in a given event. b) Cherenkov angle Plot showing the reconstructed angle of each hit detected.

4.4.5 No 1-Hit Protocol

The 1-Hit protocol was turned off so that multiple photons could hit the same pixel in a single event. When the October 2025 lens setup was used, turning of the protocol caused lots of Multi-Hits, where 3, 4 or 5 photons would hit a single pixel in a single event. Unlike that, when using a gas chamber, very few photons hit a pixel that had already been hit. In fact, the plot below showed that 96% of the detected hits were the first photons for that given pixel in that run.

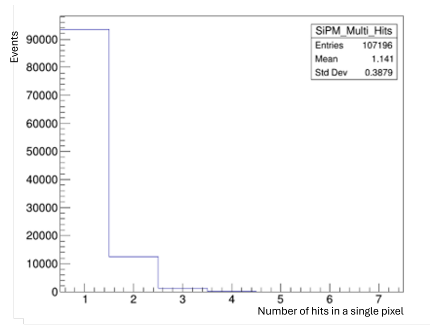

Figure 80: The number of pixels that receive 'n' number of photons in a single event.

4.4.6 PS Conditions

The aim of testing proton synchrotron conditions was to see if the PS could be used instead of the SPS and if PID was an option that could be investigated more for the 2026 Testbeam.

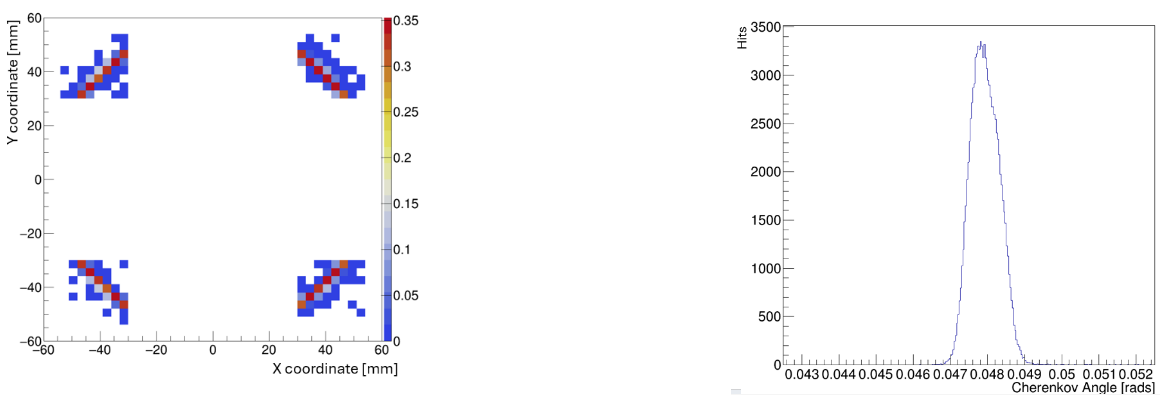

(a) (b)

Figure 83: Plots for the 'Aligned' design but under PS conditions where the momentum was $8\ GeV$. a) Pixel occupancy plot indicating the percentage chance each pixel detects a hit in a given event. b) Cherenkov angle Plot showing the reconstructed angle of each hit detected.

It was assumed that reducing the momentum to a fraction of its previous amount would cause vast affects on the data. However, as observed in [Figure 83] this was not what happened. Instead, the angular resolution only increased by 0.083 mrad, up to 0.398 mrad. Furthermore, there was no decline in occupancy, remaining at 35%. The lower momentum caused the Cherenkov angle to shift down to ~ 0.048 rad, which caused the Cherenkov ring that forms on the detector to be slightly smaller.

Overall, the difference between the PS conditions and the high momentum beam was very small, and therefore, the PS conditions could be considered for the 2026 Testbeam.

5 Conclusion

5.1 Conclusion - October 2025 Testbeam Simulation

The 2025 Testbeam simulation demonstrated that the SiPM photodetector significantly outperformed the currently used MaPMTs. Due to its superior quantum efficiency curve, the SiPM yielded an occupancy plot that was 50% more efficient (75%) compared to the 1-inch MaPMT (50%), indicating a strong case for its future adoption.

A new 200 mm lens was evaluated against the existing 150 mm lens. Although the larger lens achieved a modest improvement in angular resolution, by approximately 0.17 mrad, this came at the cost of a 14% reduction in photon occupancy. The trade-off was deemed insufficient to justify buying a new lens to replace the current one.

Timing studies for the 2025 Testbeam revealed that at low thresholds, consistent with expected experimental conditions, the effects of time walk were negligible. However, as the thresholds increased to 17.5 μA, the time walk becomes apparent, reaching 350 ps, and increasing to 550 ps at 70 μA. This highlights the importance of maintaining low thresholds in time-sensitive measurements.

5.2 Conclusion - April 2026 Testbeam Simulation

A total of seven distinct optical designs were explored in the 2026 Testbeam simulation. The optimal design, suggested to the Testbeam team, was the 'Aligned' setup; which employed a circular mirror at zero tilt to the axis, a flat mirror angled at 45°, and all optical elements aligned along the beam axis. This design achieved the second smallest Cherenkov angular resolution of 0.315 mrad, and an average ring arc occupancy of 35%, which sits on the agreed occupancy limit. Importantly, it outperformed configurations that incorporated two flat mirrors and a lens, which offered no practical advantage over a curved mirror and a single flat mirror.

The study also examined the effects of beam parameters on detector performance. A beam width of 6 mm had no impact on the results, while beam divergence introduced significant degradation. Even a small divergence of 2.5 mrad increased the resolution to 1.70 mrad, emphasising the need for tightly collimated beams.

Material studies showed that using CF_4, a gas with lower refractive index, did not work with the 'Aligned' design. The Cherenkov ring produced had a radius too small to be detected using the current SiPM positions. To accommodate such a material, the detector would require a significant increase in its length, to 1700 mm. In contrast, materials with an equal or higher refractive index to C_4F_{10} were assumed to be compatible with the existing geometries of the design.

Lastly, the impact of Proton Synchrotron low momentum conditions were assessed. This was found to have minimal impact on angular resolution and occupancy, suggesting that even non-saturated tracks may be viable for use in the Testbeam, and Particle Identification could be applicable.

6 Further Research and Development

Using a full reconstruction algorithm like the one described in section (3.4.6), would indicate how much each individual error contributes and could allow better optimisation when designing the gas chamber. Furthermore, investigating gas radiator materials such as CO_2 and gases with refractive indices similar to C_4F_{10}, to verify if they would work in the current design would be ideal. Lastly, using alternative particle types or combinations of particle types as the initial particle instead of just Pions, would allow the team to perform and test PID.

References

[1] JL Abelleira, D Amorim, SA Antipov, A Apyan, S Arsenyev, J Barranco, M Benedikt, R Bruce, F Burkart, Y Cai, et al. High-energy lhc design. In *Journal of Physics: Conference Series*, volume 1067, page 022009. IOP Publishing, 2018.

[2] Roel Aaij, Bernardo Adeva, Marco Adinolfi, Ziad Ajaltouni, Simon Akar, Johannes Albrecht, Federico Alessio, Michael Alexander, Suvayu Ali, Georgy Alkhazov, et al. Measurement of the b-quark production cross section in 7 and 13 tev pp collisions. *Physical review letters*, 118(5):052002, 2017.

[3] Dominik Muller. *Measurements of production cross-sections and mixing of charm mesons at LHCb*. PhD thesis, Manchester U., 2017.

[4] Cid Manzano Ramon Cid Vidal, Xabier. Lhcb. *Taking a closer look at LHC*.

[5] Ralf Lehnert. Cpt symmetry and its violation. *Symmetry*, 8(11):114, 2016.

[6] R Aaij, LHCb Collaboration, et al. Probing matter-antimatter asymmetries in beauty baryon decays. *Nat. Phys., doi*, 10, 2017.

[7] Boris M Bolotovskii. Vavilov–cherenkov radiation: its discovery and application. *Physics-Uspekhi*, 52(11):1099, 2009.

[8] M Adinolfi, G Aglieri Rinella, E Albrecht, T Bellunato, S Benson, T Blake, C Blanks, S Brisbane, NH Brook, M Calvi, et al. Performance of the lhcb rich detector at the lhc. *The European Physical Journal C*, 73(5):1–17, 2013.

[9] Xiao Lin, Sajan Easo, Yichen Shen, Hongsheng Chen, Baile Zhang, John D Joannopoulos, Marin Soljačić, and Ido Kaminer. Controlling cherenkov angles with resonance transition radiation. *Nature Physics*, 14(8):816–821, 2018.

[10] S. Dalla Torre, S. Levorato, G. Menon, J. Polak, L. Steiger, M. Sulc, and F. Tessarotto. A study of the rich gas refractive index. *Nuclear Instruments and Methods in Physics Research Section A: Accelerators, Spectrometers, Detectors and Associated Equipment*, 639(1):271–273, 2011. Proceedings of the Seventh International Workshop on Ring Imaging Cherenkov Detectors.

[11] R Calabrese, M Fiorini, E Luppi, L Minzoni, I Slazyk, L Tomassetti, M Bartolini, R Cardinale, F Fontanelli, A Petrolini, et al. Performance of the lhcb rich detectors during lhc run 2. *Journal of Instrumentation*, 17(07):P07013, 2022.

[12] S Easo. Overview of lhcb rich detector development. *Nuclear Instruments and Methods in Physics Research Section A: Accelerators, Spectrometers, Detectors and Associated Equipment*, 553(1-2):333–338, 2005.

[13] TL Collaboration, A Augusto Alves, LM Andrade Filho, AF Barbosa, I Bediaga, G Cernicchiaro, G Guerrer, HP Lima, AA Machado, J Magnin, et al. The lhcb detector at the lhc. *Journal of instrumentation*, 3(08):S08005–S08005, 2008.

[14] C Joram. Hpd and mapmt-segmented photon detectors for hep and beyond. In *Innovative Detectors For Supercolliders*, pages 407–426. World Scientific, 2004.

[15] F Muheim. Multianode photo multiplier tubes as photo detectors for ring imaging cherenkov detectors. *Nuclear Instruments and Methods in Physics Research Section A: Accelerators, Spectrometers, Detectors and Associated Equipment*, 502(1):52–56, 2003.

[16] Alessandro Petrolini and Steve Wotton. Proposal for lhcb rich detector enhancements during lhc long shutdown 3. 2021.

[17] Rolf Lindner. Lhcb particle identification enhancement technical design report. Technical report, 2023.

[18] "Sajan Easo". "cherenkov detectors and particle identification".

[19] LHCb Collaboration et al. Future physics potential of lhcb. Technical report, 2022.

[20] Floris Keizer. *Sub-nanosecond Cherenkov photon detection for LHCb particle identification in high-occupancy conditions and semiconductor tracking for muon scattering tomography*. PhD thesis, 2020.

[21] LHC volunteer committee. High energy physics simulation. https://lhcathome.web.cern.ch/projects/test4theory/high-energy-physics-simulations.

[22] Adele Rimoldi, on behalf ofthe ATLAS Collaboration, et al. Simulation strategies for the atlas experiment at lhc. In *Journal of Physics: Conference Series*, volume 331, page 032026. IOP Publishing, 2011.

[23] Katsuya Amako. Geant4 history. https://indico.cern.ch/event/420849/contributions/1884463/attachments

[24] E Franzoso. Italian physical society: The upgrade and performance of the lhcb rich detector. *Nuovo Cimento C*, 44:46, 2021.

[25] I Thormählen, Johannes Straub, and Ulrich Grigull. Refractive index of water and its dependence on wavelength, temperature, and density. *Journal of physical and chemical reference data*, 14(4):933–945, 1985.

[26] Yago Arosa, Elena López-Lago, and Raúl de la Fuente. Refractive index retrieval in the uv range using white light spectral interferometry. *Optical Materials*, 82:88–92, 2018.

[27] Edmund Optics. 150mm dia x 300mm focal length, pcx condesor lens. https://www.edmundoptics.eu/p/150mm-dia-x-300mm-focal-length-pcx-condenser-lens/1016/.

[28] Pengfei Yu, Ruirui Cui, Hui Xu, Cong Xu, Gangyi Zhang, Jun Zhang, and Chaoyong Deng. A novel efficient sr3in2wo9: Sm3+, eu3+ phosphor for white led applications. *Optics Laser Technology*, 163:109389, 2023.

[29] Edmund Optics. 200mm dia x 400mm focal length, pcx condesor lens. https://www.edmundoptics.eu/p/200mm-dia-x-400mm-focal-length-pcx-condenser-lens/1019/.

[30] Lishuang Ma, Guorui Huang, Zhehao Hua, Muchun Jin, Zhen Jin, Shulin Liu, Sen Qian, Lin Ren, Shuguang Si, Jianning Sun, et al. R & d of a novel single anode fast timing mcp-pmt. *Nuclear Instruments and Methods in Physics Research Section A: Accelerators, Spectrometers, Detectors and Associated Equipment*, 1041:167333, 2022.

[31] Josh Bex. "testbeam meeting february 2025". https://indico.cern.ch/event/1520390/, (restricted).

[32] S Aiello, SE Akrame, F Ameli, EG Anassontzis, M Andre, G Androulakis, M Anghinolfi, G Anton, M Ardid, J Aublin, et al. Characterisation of the hamamatsu photomultipliers for the km3net neutrino telescope. *Journal of Instrumentation*, 13(05):P05035, 2018.

[33] Hamamatsu. How does temperature affect the performance of an sipm? https://hub.hamamatsu.com/us/en/technical-notes/mppc-sipms/how-does-temperature-affect-the-performance-of-an-SiPM.html.

[34] Crystran. Optical glass (n-bk7). https://www.crystran.com/optical-materials/optical-glass.

[35] R. Abjean, A. Bideau-Mehu, and Y. Guern. Refractive index of carbon tetrafluoride (cf4) in the 300-140 nm wavelength range. *Nuclear Instruments and Methods in Physics Research Section A: Accelerators, Spectrometers, Detectors and Associated Equipment*, 292(3):593–594, 1990.

[36] Hamamatsu. S13361-3050 series. https://www.hamamatsu.com/content/dam/hamamatsu-photonics/sites/documents/$99_SALES_LIBRARY/ssd/s13361-3050_series_kapd1054e.pdf$.

[37] C D'Ambrosio, LHCb RICH Collaboration, et al. The future of rich detectors through the light of the lhcb rich. *Nuclear Instruments and Methods in Physics Research Section A: Accelerators, Spectrometers, Detectors and Associated Equipment*, 876:194–197, 2017.

[38] LHCb collaboration et al. Rich performance plots-cherenkov angle resolutions for rich 1 and rich 2. Technical report, LHCB-FIGURE-2023-007, 2023.

[39] William Moebs Samuel J. Ling, Jeff Sanny. University phsyics volume 3. https://phys.libretexts.org/Bookshelves/University$_Physics/University_Physics$